

See discussions, stats, and author profiles for this publication at: <https://www.researchgate.net/publication/230668679>

Direct Dynamics Calculation of the Kinetic Isotope Effect for an Organic Hydrogen-Transfer Reaction, Including Corner-Cutting Tunneling in 21 Dimensions

ARTICLE *in* JOURNAL OF THE AMERICAN CHEMICAL SOCIETY · AUGUST 1993

Impact Factor: 12.11 · DOI: 10.1021/ja00070a029

CITATIONS

254

READS

19

5 AUTHORS, INCLUDING:



[Donald Truhlar](#)

University of Minnesota Twin Cities

1,342 PUBLICATIONS 79,450 CITATIONS

[SEE PROFILE](#)



[Bruce C Garrett](#)

Pacific Northwest National Laboratory

295 PUBLICATIONS 11,760 CITATIONS

[SEE PROFILE](#)

University of Minnesota Supercomputer Institute Research Report UMSI 93/88

UMSI 93/88 May 1993

**DIRECT DYNAMICS CALCULATION OF
THE KINETIC ISOTOPE EFFECT FOR
AN ORGANIC HYDROGEN-TRANSFER
REACTION, INCLUDING CORNER-
CUTTING TUNNELING IN 21 DIMENSIONS**

**Yi-Ping Liu, Da-hong Lu,
Angels Gonzalez-Lafont, Donald G. Truhlar,
and Bruce C. Garrett**

1200 Washington Avenue South □ Minneapolis, Minnesota 55415

revised May 14, 1993

Direct Dynamics Calculation of the Kinetic Isotope Effect for an Organic Hydrogen-Transfer Reaction, Including Corner- Cutting Tunneling in 21 Dimensions

Yi-Ping Liu, Da-hong Lu, Angels Gonzalez-Lafont, and Donald G. Truhlar

Department of Chemistry and Supercomputer Institute,

University of Minnesota, Minneapolis, MN 55455

and Bruce C. Garrett

Molecular Science Research Center, Pacific Northwest Laboratory,

Richland, Washington 99352

Abstract. We have calculated the kinetic isotope effect of the reaction $\text{CF}_3 + \text{CD}_3\text{H}$ by a semiclassical method that gives insight into tunneling paths for hydrogen atom transfer. In particular, tunneling is treated by a new optimized multidimensional semiclassical method which is valid even for large curvature of the reaction path, and should have wide applicability. The method used in the dynamics calculations is variational transition state theory with ground-state transmission coefficients. The torsional vibrational mode of the transition state is treated as a hindered internal rotation. The calculations are made practical for a system with 27 degrees of freedom by employing the *direct dynamics* approach, i.e., the force field necessary for the dynamics calculations is evaluated “on the fly” using the neglect of diatomic differential overlap (NDDO) molecular orbital theory with semiempirical specific-reaction parameters (SRP), which are based on the standard AM1 parameterization adjusted to improve the agreement between experiment and the calculated quantities such as the vibrational frequencies of reactants and products and the classical barrier height. The kinetic isotope effects are calculated using two SRP force fields, and they are in good agreement with the experimental measurements. The picture of the corner cutting tunneling process that emerges is discussed graphically.

I. Introduction

In recent years, much progress has been made in theoretical calculations of reaction dynamics. As the size of the system of interest increases, efficient computational strategies must be adopted. The main difficulty underlying this problem is the availability of the potential energy function (PEF) necessary for dynamics calculations. The conventional approach consists of two separate steps: (i) constructing an analytic potential energy function, which provides the interaction energy and the force field at all possible geometries of the interacting system and (ii) studying the dynamics of the reaction using this potential energy function. The first step is most often accomplished by adjusting the parameters in the analytic potential energy function to fit available information, such as vibrational frequencies and barrier height, based on either *ab initio* electronic structure calculations or empirical data.¹⁻³ Since the accuracy in the prediction of the dynamics is limited by the correctness of the potential energy function, which in turn is limited by the adequacy of the functional form used for fitting, the choice of that form can be critical. As the system of interest becomes larger, so does the complexity of the fitting process, and devising adequate functional forms and determining their parameters become extremely time consuming, if it even can be done. Thus new approaches for the molecular modeling of transition state force fields are of great interest.

Recently, an alternative to the analytic PEF approach has been developed. In this approach, called direct dynamics, instead of using a pre-defined PEF, all required energies and forces for each geometry that is important for evaluating dynamical properties are obtained directly from electronic structure calculations.^{2,4-26} In some of our work^{20,22,26} employing this approach, semiempirical molecular orbital methods^{27,28} have been used because they are much less expensive than *ab initio* calculations. Semiempirical molecular orbital methods have been broadly applied in various fields of chemistry, especially in organic chemistry. The most successful versions of these methods are based on the neglect of diatomic differential overlap (NDDO),²⁷⁻³⁰ and well known parameter sets have been

adjusted to the enthalpy of formation and geometries for selected, but large, sets of molecules.²⁸⁻³⁰ Since not all the measurables chosen in the fitting process are crucially relevant to the dynamics of a specific system, the accuracy for a specific system may be unnecessarily compromised by using parameters that were adjusted to reduce the overall error for all the test data in the set; thus there is room for improvement by fitting the parameters specifically to the important properties for the reaction of interest. When we perform such adjustments to model the energies and forces in a specific system or a small set of closely related reactions, the resulting semiempirical approach is called NDDO-SRP,^{20,22} where SRP denotes specific reaction parameters. In this article we present an NDDO-SRP direct dynamics study on the reactions of $\text{CF}_3 + \text{CD}_3\text{H} \rightarrow \text{CF}_3\text{H} + \text{CD}_3$, and $\text{CF}_3 + \text{CD}_3\text{H} \rightarrow \text{CF}_3\text{D} + \text{CD}_2\text{H}$. Reaction rate constants are calculated based on variational transition state theory³¹⁻³⁹ with semiclassical multidimensional tunneling corrections with and without the assumption of vibrational adiabaticity.^{26,33-37,40-45}

A considerable amount of kinetic data has been obtained concerning the reaction of CF_3 with alkanes.⁴⁶⁻⁵⁴ We are especially interested in the reactions of trifluoromethyl radical with methane and deuterated methane because they are prototype hydrogen-transfer reactions, and they have several interesting features. They involve transfer of a light atom between two heavy moieties, the so-called heavy-light-heavy (HLH') mass combination, which is important for proton and hydride transfer as well. The HLH' -type of reaction may involve significant tunneling, and the reaction-path curvature must be taken into account in the calculation of tunneling. The reaction path of a hydrogen-transfer reaction is strongly coupled to the stretch vibrational mode of the reactant and product, LH and LH' in this case, because they involve mainly the motion of the light atom, and for a light transferred atom in a bimolecular reaction this results in large curvature of the reaction path in the mass-scaled coordinates (defined in the theory section) for which curvature is most meaningful.³⁴ The mass combination, the nearly zero heat of reaction, and the significant (~14 kcal/mol) barrier height obtained from an Arrhenius fitting of experimental rate

constants,⁴⁶⁻⁵⁰ lead us to expect a dominant contribution from tunneling^{36,40} at low temperatures, and the tunneling process may involve important contributions from tunneling into excited states.^{41,42} Thus, in the present paper we allow for these contributions by employing a semiclassical method for the transmission coefficient, called the microcanonical optimized multidimensional (μ OMT) tunneling approximation. In the μ OMT method, tunneling probabilities in the small-curvature and large-curvature limits are calculated using the centrifugal-dominant semiclassical adiabatic ground-state (CD-SCSAG) and large-curvature ground-state, version 3 (LCG3)^{34,43,44} approximations, respectively, and the optimal tunneling probabilities are approximated as the larger of the two calculated limiting cases, which choice is justified by the criterion of least action,⁵⁵ as discussed in Section II.

Another important feature of the present reaction is that one of the vibrational modes of the generalized transition state (GTS) is a torsion. The torsional mode is common to large organic molecules, and including anharmonicity⁵⁶ in the partition function for this mode can potentially make a large difference in the calculated rate constant. Thus we apply a new hindered rotor approximation⁵⁷ to evaluate these partition functions.

Prior to our calculations, there have been other attempts to model this group of reactions using conventional transition state theory. Sharp and Johnston⁴⁷ used a London-Eyring-Polanyi-Sato (LEPS)⁵⁸ potential. Their objective was to test the transition state theory and especially to test how important it is to include all the vibrational degrees of freedom explicitly or implicitly in the calculation. Their work is also one of very few early attempts to include multi-dimensional effects in tunneling calculations. Brown *et al.*⁵⁹ calculated kinetic isotope effects (KIEs) using the MNDO²⁸ parameterization; in particular they calculated the ratio of rate constants for $\text{CF}_3 + \text{CH}_4$ and $\text{CF}_3 + \text{CD}_4$ using conventional transition state theory. The calculated barrier is too high in their calculation, and tunneling is not included. We note that the predicted energy of reaction has a significant deviation from experiment for all standard²⁸⁻³⁰ NDDO parameterizations,

including MNDO; as a consequence, the shape of the barrier is not realistic, and one must be cautious about conclusions drawn from dynamical studies in such cases.

A theoretical investigation including all degrees of freedom and a reliable estimate of the tunneling contribution with a barrier height that leads to good agreement with the experimental absolute rate constants should lead to a more complete understanding, and this is the goal of the present paper. In particular, we include all 27 degrees of freedom in our treatment of the overbarrier dynamics and all 21 internal degrees of freedom in our treatment of the tunneling. The energies and the force field are obtained from two new NDDO-SRP models, which are parameterized to give reasonable barrier height and better agreement in the vibrational frequencies of reactants and products to experiment.

This paper is organized as follows. A brief review of the NDDO method, variational transition state theory (VTST), the hindered rotor approximation, and the multidimensional semiclassical tunneling methods is given in the theory section. Details of the calculations are given in the computational methods section. The following sections give results, discussion, and conclusions.

II. Theory

NDDO. The potential energy surface for the present calculations is obtained by semiempirical molecular orbital using the NDDO approximation^{27-30,60} for the unrestricted Hartree-Fock equations⁶¹ in a minimal basis of Slater-type atomic orbitals. In this approach, the Fock matrix, of which the molecular orbitals are eigenvectors, involves the following terms: (i) one-center two-electron repulsion integrals, (ii) two-center two-electron repulsion integrals and two-center one-electron core resonance integrals, $\beta_{\mu\lambda}$, between orbitals on different centers, (iii) two-center one-electron core attraction integrals between an electron in the distribution $\phi_{\mu}\phi_{\nu}$ at atom A and the core of atom B, and (iv) one-center one-electron energies, $U_{\mu\mu}$, which are the sum of the kinetic energy of an electron in ϕ_{μ} at atom A and its potential energy due to the attraction by the core of atom A.

Semiempirical methods reduce the computational effort by expressing the various terms in the Fock matrix in parameterized forms fit to experimental data.²⁸⁻³⁰ In this work, we start with the AM1 (Austin model 1) parameterization.²⁹ In this model two parameters, the orbital exponents ζ_s and ζ_p , are necessary to specify the basis for an element like C or F, and one orbital exponent, ζ_s , specifies the basis for H atoms. The two-center one-electron resonance integrals, $\beta_{\mu\lambda}$, are approximated by

$$\beta_{\mu\lambda} = \frac{(\beta_{\mu}^A + \beta_{\nu}^B)}{2} S_{\mu\lambda} \quad (1)$$

where β_{μ}^A and β_{ν}^B are parameters, and $S_{\mu\nu}$ is the overlap integral of two Slater orbitals.

The parameters ζ_s , ζ_p , U_{ss} , U_{pp} , β_s , β_p , and other parameters were adjusted for each atom in the AM1 model so that the theory gives good approximations to experimental heats of formation, gradients, and geometries for a selected but large set of molecules.²⁹

The total energy of a system, E_{total} , is the sum of the electronic energy and the core-core repulsion energy. Note that E_{total} as a function of geometry is the Born-Oppenheimer potential surface V .

Variational Transition State Theory. The variational transition state theory rate constant is the minimized value obtained by varying the location of the generalized transition state along a reference reaction path. This minimizes the error due to "recrossing" trajectories.^{32,37} The choice we make for the reference path is the minimum energy path (MEP) obtained by following the steepest descent of the potential from the saddle point in a mass-weighted or mass-scaled coordinate system,⁶²⁻⁶⁶ scaled to a reduced mass μ . (In the present paper we set μ equal to 1 amu. This arbitrary choice has absolutely no effect on calculated observables, but choosing a physical value makes distances in the mass-scaled system correspond more closely to physical distances.) We denote the signed distance along the MEP through mass-scaled coordinates as s ; this coordinate is negative and positive on the reactant and product sides respectively. The

Born-Oppenheimer potential energy along the MEP is called $V_{\text{MEP}}(s)$. The level of variational transition state theory used in the present paper is canonical variational theory³¹ (CVT) with a transmission coefficient^{26,33,44} that accounts for tunneling and nonclassical reflection.

For a canonical ensemble, the hybrid (i.e., classical reaction path motion with other degrees of freedom quantized) CVT rate constant for a bimolecular reaction is given by³⁴

$$\begin{aligned} k^{\text{CVT}}(T) &= \min_s k^{\text{GT}}(T, s) \\ &= \sigma \frac{\tilde{k}T}{h} \frac{Q^{\text{GT}}(T, s_*^{\text{CVT}})}{\Phi^R(T)} e^{-V_{\text{MEP}}^{\text{CVT}}/\tilde{k}T} \end{aligned} \quad (2)$$

where $k^{\text{GT}}(T, s)$ is the hybrid rate constant for temperature T and a generalized transition state (GTS) located at s , s_*^{CVT} is the value of s at which $k^{\text{GT}}(T, s)$ has a minimum, i.e., the location of the CVT transition state, σ is the symmetry factor (omitted from rotational partition functions) which accounts for the reaction path multiplicity, \tilde{k} is the Boltzmann constant, h is Planck's constant, $V_{\text{MEP}}^{\text{CVT}}$ is the Born-Oppenheimer potential $V_{\text{MEP}}(s)$ on the MEP at s_*^{CVT} , $Q^{\text{GT}}(T, s_*^{\text{CVT}})$ is the internal quantum partition function for a generalized transition state at a value $s = s_*^{\text{CVT}}$ of the reaction coordinates with $V_{\text{MEP}}^{\text{CVT}}$ as the local zero of the energy, and Φ^R is the reactant quantum partition function per unit volume with respect to the overall zero of energy taken as the equilibrium potential of reactants infinitely apart for bimolecular reactions. Φ^R is a product of the relative translational energy partition function per unit volume and internal partition functions for the reactants. If the generalized transition state rate constant is evaluated at the saddle point ($s = 0$) instead of the variationally optimized s_*^{CVT} , then $V_{\text{MEP}}^{\text{CVT}}$ is replaced by the classical barrier height V^\neq , and Eq. (2) reduces to conventional transition state theory (denoted TST).

To include quantum effects for motion along the reaction coordinate, we multiply $k^{\text{CVT}}(T)$ by a ground-state transmission coefficient, $\kappa^{\text{CVT}/G}$, which primarily corrects for

the influence of tunneling on the rate constant and for nonclassical reflection effects. That is, the quantized rate constant, $k^{CVT/G}(T)$ is³⁴

$$k^{CVT/G}(T) = \kappa^{CVT/G}(T) k^{CVT}(T) \quad (3)$$

Partition Functions. By assuming the electronic, rotational, and vibrational degrees of freedom are separable, each internal partition function, Q , may be rewritten as the product of three factors which are called Q_{el} , Q_{vib} , and Q_{rot} . Since the rotational energy levels are generally closely spaced, little accuracy is lost if we approximate the quantal rotational partition function by the corresponding classical one. For the present study the GTS electronic partition is assumed to cancel the electronic contribution to $\Phi^R(T)$. The vibrational partition function is evaluated in the framework of the independent normal mode (INM) approximation, which means that we neglect anharmonic mode-mode couplings so that the vibrational partition function is separable. Thus the vibrational partition function for a GTS can be expressed as:

$$Q_{vib}^{GT}(T,s) = \prod_{m=1}^{3N-7} Q_{vib,m}^{GT}(T,s) \quad (4)$$

where N is the number of atoms (9 for reactions in the present study), and m labels the vibrational mode. We apply a projection operator to the force constant matrix in mass-scaled cartesians^{34,67,68} to project out the overall translational and rotational motions for stationary configurations and also the motion along the reaction path for a generalized transition state. The generalized normal mode coordinate, Q_m , and the quadratic force constant, $k_{mm}(s)$, for $m = 1$ to $3N-7$ are then obtained by diagonalizing the projected force constant matrix, and the generalized normal mode frequency $\omega_m(s)$ of mode m is calculated by

$$\omega_m(s) = [k_{mm}(s)/\mu]^{1/2} \quad (5)$$

For the reactions in the present study, all reactant vibrations and all but one of the GTS vibrations are treated harmonically in cartesians;^{34,67,68} the other GTS vibration is a torsional motion which is treated as an internal rotation.

Rotational partition functions are calculated without symmetry numbers. Instead, all symmetry numbers are included in σ (the values for the reactions in this paper are given and explained in details in the computational section).

Hindered Rotors. We calculate the partition function for the vibrational mode corresponding to torsional motion by interpolation between the limits for harmonic oscillators and for free rotors,⁵⁷

$$Q_m^{HR}(T,s) = Q_m^H(T,s) f_m(T,s) \quad (6)$$

where the superscripts HR and H stand for hindered rotor and harmonic oscillator respectively, $Q_m^H(T,s)$ corresponds to the zero of energy at the bottom of the parabolic part of the potential for the mode m treated as a hindered rotor, and $f(T,s)$ is an interpolating function given by

$$f_m(T,s) = \tanh\left(Q_m^{FR}(T,s) \frac{\hbar\omega_m(s)}{kT}\right) \quad (7)$$

where $Q_m^{FR}(T,s)$ is the partition function obtained by the free rotor approximation, and $\omega_m(s)$ is the harmonic frequency. For a σ_I -fold internal rotation, the potential in the internal rotational mode is approximated by

$$V(s,\phi) = V_{MEP}(s) + [\omega_m(s)]^2 I(s)(1 - \cos \sigma_I \phi), \quad (8)$$

where the reduced effective moment of inertia in Eq. (8) is defined as⁶⁹

$$\bar{I}(s) = \frac{1}{\sigma_I^2} \frac{I_1(s)I_2(s)}{[I_1(s)+I_2(s)]} \quad (9)$$

where $I_1(s)$ and $I_2(s)$ are the moments of inertia of the two subgroups of the species of interest which are undergoing relative rotation. The internal rotational axis is defined in the direction of the angular momentum of one of two mutually rotating subgroups, i.e., in the direction of the cross product of the generalized normal mode eigenvector and the position vector. Let the internal rotational axis be the z axis in the mass-scaled coordinate system.

Then the moment of inertia of a subgroup is given by

$$I_i(s) = \mu \sum_{A \in i} (x_A^2 + y_A^2) \quad (10)$$

where (x_A, y_A, z_A) is the mass-scaled position vector of atom A belonging to subgroup i which can be 1 or 2, and μ is the reduced mass used to define the mass-scaled coordinates.

Multidimensional Semiclassical Tunneling Method. A ground-state transmission coefficient,^{32,70} $\kappa^{CVT/G}(T)$, for the CVT rate constant is defined as the ratio of the thermally averaged quantal transmission probability, $P^G(E)$, for the reaction in the ground state, to the thermally averaged classical transmission probability, $P_C^G(E)$ for classical reaction-coordinate motion along the one-dimensional ground-state barrier, i.e.,

$$\kappa^{CVT/G}(T) = \frac{\int_0^\infty P^G(E)e^{-E/\tilde{k}T} dE}{\int_0^\infty P_C^G(E)e^{-E/\tilde{k}T} dE} \quad (11)$$

where $P_C^{CVT/G}(E)$ is zero when the energy of the system is below the classical threshold energy implied by CVT and is unity otherwise. To be consistent with k^{CVT} [see Eq. (3)], we take the classical threshold energy as $V_a^G(s = s_*^{CVT})$.

Several semiclassical tunneling approximations are available to calculate $P^G(E)$. The minimum energy path semiclassical adiabatic ground-state (MEPSAG)^{64,70} method assumes that the reaction path has negligible curvature so that the tunneling path essentially coincides with it. Transmission coefficients $\kappa^{CVT/G}(T)$ calculated by this method are labeled ZCT (“zero-curvature tunneling”). However, tunneling occurs on the concave side of the MEP when the reaction path possesses curvature.^{1,36,64,71,72} This is called corner cutting. A practical method for including this effect in tunneling processes of polyatomic molecules is the centrifugal-dominant small-curvature semiclassical adiabatic ground-state (CD-SCSAG) approximation,^{26,43} which we will call SCT for “small curvature tunneling.” This is a generalization of the Marcus-Coltrin⁷¹ approximation in which the tunneling path is distorted from the MEP out to a concave-side vibrational turning point in the direction of the internal centrifugal force.⁴³ Both ZCT and SCT formalisms are based on the assumption of vibrational adiabaticity. In particular, $P^G(E)$ is calculated in these methods using an effective potential corresponding to adiabatic evolution of the vibrational energy from the ground state of the reactants to the ground state of the products. This effective potential is the vibrationally adiabatic ground-state potential defined by

$$V_a^G(s) = V_{MEP}(s) + \frac{1}{2} \hbar \sum_{m=1}^{3N-7} \omega_m(s). \quad (12)$$

Since a hindered rotor approximation is applied for evaluating the partition function of the internal rotational mode, a consistent treatment is necessary for calculating the contribution from this mode to $V_a^G(s)$. One can see that the function f in Eq. (6) converges to 1, and

hence Q_m^{HR} converges to Q_m^H as the temperature goes to zero. Therefore a zero point energy of $\frac{1}{2} \hbar \omega_m(s)$ is assigned to hindered internal rotational modes in our calculations.

Computational details of the MEPSAG and CD-SCSAG methods are given elsewhere.^{34,43}

We also applied the large-curvature-ground-state approximation, version 3,^{34,41-45,55,73} (LCG3), which we will call LCT for “large curvature tunneling.” In the LCG3 method, the reaction is assumed to proceed vibrationally adiabatically prior to and after tunneling, but no vibrational adiabaticity is assumed during the tunneling processes, and tunneling into excited vibrational states of the product in the exoergic direction is explicitly included in a quasidiabatic representation. In particular, on the reactant side of the MEP in the exoergic direction, we include only the ground state,^{32,34,44,70} while on the product side of the MEP in the exoergic direction all the accessible vibrationally-excited states of a quasidiabatic mode excited by the tunneling process are included.^{41-43,45} (In early presentations of the theory for polyatomics,^{34,44} only the ground state was considered on both sides of the reaction path.) The quasidiabatic mode, called the p mode, is defined as a linear combination of all the generalized normal modes that are coupled to the tunneling path.⁴³ The LCG3 tunneling formulas include contributions from all straight-line tunneling paths⁴⁰ with equal pre- and post-tunneling reaction coordinate components of the kinetic energy for all accessible vibrational states n_p of the p mode. The contributions from tunneling paths with various termini are averaged by using a quasiclassical distribution function. That is, the primitive tunneling amplitudes are given by

$$T_i(E, n_p) = \left| \int_{s_i(E)}^{\infty} V_R^{-1}(E, \tilde{s}_i, n_p) \tau^{-1}(\tilde{s}_i, n_p) e^{-\theta(\tilde{s}_i, n_p)} \sin \chi(\tilde{s}_i, n_p) d\tilde{s}_i \right|, \quad (13)$$

where E is the total energy, $i = 0, 1$ for tunneling path termini \tilde{s}_i on the reactant and the product side of the MEP, respectively, s_0 and s_1 are the classical translational turning points corresponding to tunneling energy E and are determined by

$$E = V_a^G(s_0) = V_a^g(n_p, s_1; s_0), \quad (14)$$

where

$$V_a^g(n_p, s; \tau_0) = V_a^G(s) + n_p \hbar \omega_p(s; \tau_0), \quad (15)$$

$V_R(E, \tilde{s}_i, n_p)$ is the local speed along the reaction coordinate at \tilde{s}_i , $\tau(\tilde{s}_i, n_p)$ is the vibrational period, $\chi(\tilde{s}_i, n_p)$ is the angle between the tunneling path and the MEP where the tunneling path intersect at \tilde{s}_i , and $\theta(\tilde{s}_i, n_p)$ is the action integral for tunneling into the n_p excited state, and is evaluated along the straight-line tunneling path with the tunneling terminus \tilde{s}_i .²⁶ Note that s_0 is negative and s_1 is positive; also note that the upper integration limit is $-\infty$ for $i = 0$ and $+\infty$ for $i = 1$ for an exoergic reaction.

Equation (13) gives the tunneling amplitude for tunneling initiated by the vibrational motion normal to the reaction path [which is the reason for the factor $\sin\chi(\tilde{s}_i, n_p)$ in Eq. (13)]. The contribution from tunneling along the reaction path is also included.^{34,43} The primitive tunneling probability is summed over final states with vibrational quantum number n_p .⁴³ The integration in Eq. (13) may lead $P_{\text{prim}}(E, n_{\max})$ to be greater than 0.5 or even greater than 1, but the transmission probability should be 0.5 at the classical threshold. Therefore $P_{\text{prim}}(E, n_{\max})$ is uniformized⁷⁴ by Eq. (19) of Ref. 45 to the correct limit for all value of n_{\max} from 0 up to the quantum number of the highest accessible state. The largest of these uniformized values at each E is accepted as the final approximation and is called $P^G(E)$. The transmission probability is taken as unity when $E > V_a^{\text{AG}} - E_0$, where V_a^{AG} is the maximum of $V_a^G(s)$, the vibrationally adiabatic ground-state potential along the MEP, and E_0 is the quantal threshold energy, i.e., the larger of the adiabatic ground-state energies of the reactants and products. Substituting the expression for $P^G(E)$ in the different energy ranges into Eq. (11), we obtain the transmission coefficient $\kappa^{\text{CVT/LCG3}}(T)$.

Optimized Multidimensional Tunneling Approximation. Of the three tunneling approximations presented above, the ZCT method is the simplest; it involves multidimensional effects in the effective potential, but it neglects the effect of reaction-path curvature. The CD-SCSAG^{26,43} method is a multidimensional tunneling approximation that is valid for the case of small reaction-path curvature. Unlike the earlier SCSAG method,^{33,34} it includes the effect of mode-mode coupling on the extent of corner cutting, and so it is valid even for systems with significant reaction-coordinate curvature in several modes like the present system, provided that curvature is small enough. The LCG3 method^{34,43-45} specifies tunneling paths explicitly in a multidimensional context. It is a general method but may not be the optimal method for small and medium curvature cases. Ideally the most general and optimal method is to employ a criterion of least imaginary action,⁵⁵ by which the tunneling path may be more fully optimized. However, the least-action method would require considerable computational effort for polyatomic systems, and so far it has been applied only to atom-diatom reactions. Instead, we have proposed a simpler optimized multidimensional tunneling (OMT) approximation.⁷³ In the previous application,⁷³ the optimization was carried out in a canonical ensemble (canonical optimized multidimensional tunneling, COMT), and here we propose a version based on microcanonical optimization (microcanonical optimized multidimensional tunneling, μ OMT method).

In the μ OMT method we write

$$P^G(E) = \max \begin{cases} P^{LCT}(E) \\ P^{SCT}(E) \end{cases} \quad (16)$$

where $P^{LCT}(E)$ and $P^{SCT}(E)$ are calculated by the LCG3 and CD-SCSAG methods respectively. Substituting the expression for $P^G(E)$ in the different energy ranges into Eq. (11), we obtain the transmission coefficient $\kappa^{CVT/\mu\text{OMT}}(T)$. We may simplify the

μ OMT method and select an optimal tunneling approach at canonical level. This results in the COMT method, for which we write

$$\kappa^{\text{CVT/COMT}}(T) = \max \begin{cases} \kappa^{\text{CVT/LCT}}(T) \\ \kappa^{\text{CVT/SCT}}(T) \end{cases} \quad (17)$$

where $\kappa^{\text{CVT/LCT}}(T)$ and $\kappa^{\text{CVT/SCT}}(T)$ are calculated by the usual LCG3 and CD-SCSAG method respectively.⁷³

III. Computational Methods

As mentioned above, rate constants, k , were calculated by canonical variational transition state theory with a transmission coefficient based on the microcanonical optimized multidimensional tunneling calculation. The results with and without tunneling are denoted CVT/ μ OMT and CVT, respectively, and for comparison we also carried out a conventional transition state theory^{75,76} calculation, without tunneling, denoted TST. The conventional calculations, like the variational ones, treat the torsional mode as a hindered rotator.

Symmetry is included, as usual,^{34,43} by omitting symmetry numbers in rotational partition functions and by including the factor σ^{3g} ,^{77,78} in Eq. (2) and σ_I^{6g} in Eq. (9) for internal rotation. In the present study, the symmetry factor σ is simply the product of the symmetry numbers of the reactants divided by the symmetry number of the transition state (or the generalized transition state). For example, σ is 9 for reaction $\text{CF}_3 + \text{CD}_3\text{H} \rightarrow \text{CF}_3\text{D} + \text{CD}_2\text{H}$. For the H-transfer reaction, σ is 3. The symmetry factor σ_I for internal rotation is 3 for the saddle point and all generalized transition states of both the H- and D-transfer reactions.

In all cases, hessians were obtained by taking central differences of the gradients in cartesian coordinates, and the finite difference stepsize used is 0.011 a_0 .

The Euler method with stabilization⁷⁹⁻⁸¹ was employed to obtain the MEP; in particular we employed the ES1 method as described in ref. 63. Gradients were calculated

every 0.002 a_0 or 0.0025 a_0 in mass-scaled coordinates, and the hessian matrix was calculated every 0.005 a_0 . Convergence checks were performed for both these stepsizes, and they were found to be adequate for an accuracy of 5% in the calculated rate constants. The stabilization stepsize⁸¹ was 0.001 a_0 , and the tolerance in the allowed vector difference between successive normalized gradients was set equal to 1×10^{-8} .

Details of numerical procedures are provided in previous papers^{34,43,45,82} and summarized above in the theory section. The calculations were carried out with the computer program MORATE (version 4.5/P4.5.1–M5.03), also described elsewhere.⁴⁵

Absolute reaction rate constant. All available experimental measurements of the rate coefficient of the hydrogen abstraction reaction of trifluoromethyl radical with methane and deuterated methane are relative rate coefficients referenced to the high-pressure limit of the rate coefficient for the radical recombination reaction $2\text{CF}_3 \rightarrow \text{C}_2\text{F}_6$. For fitting the NDDO-SRP parameters and for comparison to experiment, we needed to place the experimental rate constants on an absolute scale. To obtain the absolute rate coefficients we need to know the recombination rate coefficient at its high pressure limit, $k_{r,\infty}$. We interpolated between the available $k_{r,\infty}$ at 300 K⁸³ and at 1300 K⁸⁴ with an Arrhenius equation in which the Arrhenius pre-exponential factor is $3.9 \times 10^{-11} \text{ cm}^3 \text{ molecule}^{-1} \text{ s}^{-1}$ and the activation energy is 1.36 kcal/mol (although in most experimental references,^{46–50} $k_{r,\infty}$ is assumed to be independent of temperature). The estimated value of $k_{r,\infty}$ at 626.8 K plays a prominent role in the parameterization; this treatment yields $1.31 \times 10^{-11} \text{ cm}^3 \text{ molecule}^{-1} \text{ s}^{-1}$ for this critical value.

IV. Results and Discussions

Parameterization. The experimental energy of reaction, ΔE , which equals E_{total} of products minus E_{total} of reactants, is estimated from the enthalpy of formation⁸⁵ of reactants and products at 0 K by correcting for the change in harmonic zero-point energies,⁸⁵ and the energy of reaction is found to be -0.72 kcal/mol. In comparison, the calculated energies of reaction are -11.5, -10.7, and -12.5 kcal/mol using the MNDO,²⁸ AM1,²⁹ and PM3³⁰ hamiltonians, respectively. Thus all three standard parameterizations

predict very asymmetric barrier profiles because of this error in ΔE . In adjusting the parameters to achieve better agreement with experiment for properties at stationary configurations and hence a more realistic barrier profile, it is desirable to obtain an SRP model with the least perturbation to the one of the standard ones, because, in our experience, large perturbations in parameters can make geometries or vibrational frequencies unrealistic. Since the deviation in the energy of reaction is the least for AM1, we therefore started with the AM1 parameterization to obtain the SRP parameters. Furthermore, the predictions to the dynamics should not be overly sensitive to which parameters are selected to be modified. To monitor the latter requirement, we compare results from two different SRP models that are fits to the same empirical data.

In order to adjust the parameters in the NDDO-SRP method, we chose to reproduce two experimental data. First we required that ΔE be correct. Second we fit the rate constant, $k_D^{CVT/\mu OMT}$, of the reaction $CF_3 + CD_3H \rightarrow CF_3D + CD_2H$ to the experimental result⁴⁷ at 626.8 K. Note that the reaction multiplicity is included in the symmetry factor of $k_D^{CVT/\mu OMT}$, and the rate constant for transferring a single D atom is $\frac{1}{3}k_D^{CVT/\mu OMT}$. In the following, k_D is referred to as the rate constant for the overall reaction, and the rate constant for transferring a single deuterium will be explicitly indicated when relevant for discussion purposes.

Two sets of optimized parameters were obtained, trying in addition to fit these two data, to improve the accuracy of at least one of the CF_3 -H or CH_3 -F bond energies and some of the reactant and product vibrational frequencies, as well as restricting all the changes in the parameters to be less than 10% of the original AM1 values. Six parameters are modified in each SRP model, as tabulated in Table I. Two parameters, ζ_s for F and β_s for H, are adjusted to the same values in both SRP models, and the other adjusted parameters different in their identity or their values in the two SRP models.

Table II gives the calculated vibrational normal mode frequencies of CH_4 , CF_3 , CH_3 , and CF_3H , and it compares these to experiment. Table III compares the C-H bond

dissociation energy of CH₄ and of CF₃H, the energy of reaction, and the root-mean-square of the deviation of frequencies from experiment. It is clear from Table III that both SRP models fit the energy of reaction to better than one-half kcal/mol, with the SRP-2 model being slightly closer to experiment. The quality of the fits to the bond dissociation energies and frequencies is very similar. The root-mean-square deviations of the frequencies calculated using the two SRP models from experiment are 11–12% less than calculated by AM1. The maximum deviation in frequency is also smaller in the two SRP models than in AM1.

We compare geometries of the reactants and products calculated from the AM1, SRP-1, and SRP-2 with experiment⁸⁴ in Table IV. The geometries are slightly closer to experiment than those calculated by AM1.

Stationary points. No experimental data is available for properties at the saddle point. The adjustment of the parameters to make $k_D^{CVT/\mu\text{OMT}}$ fit the experimental D-transfer rate constant at 626.8 K ensures a reasonable value for the classical barrier height, i.e., the difference in the Born-Oppenheimer potential of the saddle point and that of the reactants. Table V compares the geometry of the saddle point from AM1 and the two SRP models. All three calculated saddle points are eclipsed structures with C_{3v} symmetry; the coordinates for the transition state are defined in Figure 1. Table V shows, as expected from the discussion above, that the AM1 saddle point is much more asymmetric than the ones calculated with parameters that have ΔE values much closer to zero (and to experiment). In addition, there is encouraging agreement between the two SRP saddle point geometries, indicating that this feature is not overly sensitive to the choice of which NDDO parameters were varied. Table VI lists the normal mode frequencies of CF₃–H–CH₃, which characterize the force field in the vicinity of the saddle point. Examination of the table indicates that the force fields from the two models with disjoint sets of adjusted parameters are very similar. This is also encouraging.

Barrier shape. Figure 2 presents the Born-Oppenheimer potential along the MEP for the H-transfer reaction for the two parameterizations, and Figure 3 presents the adiabatic ground-state potential, $V_a^G(s)$, along the MEP. Again, there is good agreement between results from the two SRP models. The SRP-2 parameterization leads to a slightly thinner barrier. The shoulders in Figure 4 result from competition between a decreasing potential energy and an increasing zero point contribution as far less marked for the D transfer.

Anharmonicity. The lowest frequency mode corresponds to a three-fold internal rotation of the methyl group with respect to the trifluoromethyl group. The barrier associated to the internal rotation is 0.043 kcal/mol for SRP-1 and 0.036 kcal/mol for SRP-2. Since the internal rotation is uncoupled from the overall rotation, the internal rotation axis must go through the center of mass. For the H-transfer reaction in the present study, the internal rotation axis is the straight line that passes through the two carbons and the migrating H, and these atoms will not contribute to the reduced moment of inertia regardless how the GTS is divided into two subgroups. For the D-transfer reaction, however, the center of mass of the saddle point or the generalized transition states, $\text{CF}_3\text{---D---CD}_2\text{H}$, is not along the C-D-C axis, and the internal rotation axis deviates slightly from the C-D-C axis. Thus the carbons and the migrating deuterium contribute to the reduced moment of inertia, and the contribution depends on how the GTS is divided into two subgroups. The division we used for the final calculations corresponds to CF_3D and CD_2H on the product side of the MEP and to CF_3 and CD_3H on the reactant side of the MEP. We performed calculations for cases where the generalized transition state configuration is divided as $\text{CF}_3\text{D}/\text{CD}_2\text{H}$ along the whole reaction path or divided as $\text{CF}_3/\text{CD}_3\text{H}$ along the whole path, and we found the maximum difference in the calculated k^{CVT} is under 2%, which is negligible.

The effect of including anharmonicity is significant. The partition function of the torsional mode at the saddle point configuration at 626.8 K calculated harmonically is about

2.98 and 3.11 times bigger than the value calculated with the hindered internal rotor approach in the SRP-1 and SRP-2 models respectively. This result is expected for the following reason. At high temperature, the hindered torsional mode approaches the free rotor limit. The multiplicity due to symmetry is taken into account in the free rotor approximation, i.e., it is included in the internal rotational symmetry number, σ_I^{69} [see Eq. (9)]. On the other hand, the harmonic approach will overestimate the partition function by including points within σ_I indistinguishable parts of the phase space. Thus it is not surprising that the harmonic partition function is about 3 times bigger than the one calculated by the hindered rotor approximation for a three-fold internal rotor at high temperature. At 200 K the harmonic partition function of this mode at the saddle point is about 1.82 and 1.89 times as large as the hindered-rotor partition function for the SRP-1 and SRP-2 models respectively. This shows harmonic approximation overestimates the partition function for this mode significantly throughout the temperature range considered in the present study.

Recrossing. Rate constants calculated by TST and CVT at 626.8 K are compared in Table VII. The difference between the TST and CVT values is a measure of how much recrossing occurs at the conventional transition state, i.e., the saddle point. Variational optimization of the transition state location reduces the rate constants for H transfer by 15–19% and those for D transfer by 21% at 626.8 K

Kinetic isotope effect. Table VII also contains the rate constants and the kinetic isotope effects from experiment and from the present CVT/ μ OMT calculation at 626.8 K. (Note that $k_D^{\text{CVT}/\mu\text{OMT}}$ was fit to experiment at this temperature.) The predicted rate constants for $\text{CF}_3 + \text{CD}_3\text{H} \rightarrow \text{CF}_3\text{H} + \text{CD}_3$ agree with experiment within 11%, which is better than the reliability of either the dynamical calculations or the experimental results. With the Arrhenius fit of $k_{r,\infty}$ explained in the computational methods section, absolute reaction rate constants are calculated from the relative rate constants measured by Sharp and Johnston,⁴⁷ and they are plotted in the Figures 4 and 5, which also include the present

calculations. The figures show that the predicted rate constants in the two SRP models are in good agreement with the experimental measurements throughout the entire temperature range. Figure 6 is a plot of the kinetic isotope effect vs. $1000/T$. The experimental KIEs plotted in Figure 8 are taken directly from Sharp and Johnston.⁴⁷ They measured the relative H- and D-transfer reaction rate constants in the same set of experiments, and these KIEs are expected to be more reliable than individual reaction rate constants because certain systematic errors are expected to cancel in the KIEs. The two SRP models give reasonable predictions of KIEs. The SRP-2 model does slightly better than SRP-1. The excellent agreement of theory and experiment for the kinetic isotope effect is a major success of the present calculations, confirming the usefulness of combining NDDO-SRP procedures and variational transition state theory with OMT tunneling. Notice from Table VII that the KIEs calculated without tunneling are about 35% too small even at relatively high temperature of 626.8 K.

Tunneling. Table VIII presents the μ OMT transmission coefficients for the H-transfer reaction from the two SRP models for a few selected temperatures. The experimental H-transfer rate constant and KIE at 367.8 K are also tabulated. The KIEs can be factorized⁸⁶ into contributions from tunneling and from the rest. We tabulate these two factors as well as the KIEs themselves in Table VIII. Compared to the experimental H-transfer rate constant at 367.8 K, the predicted rate constants from the two SRP models are slightly outside the 2σ error bars in the experimental rate constants. The experimental error bars are estimated from the 2σ error bars in the reported activation energy of the relative H-transfer rate constants,⁴⁷ but of course such error bars do not include possible systematic errors, and the contribution from the errors in the recombination reaction is *not* included. Therefore, the agreement between the calculated H-transfer rate constant and experiment is satisfactory.

The KIEs computed from kCVT in the two SRP models agree with each other within 5% at all temperatures tabulated in Table VIII. This is consistent with the fact that

the adiabatic ground-state potentials and force fields in the vicinity of the saddle point from the two models agree well with each other. As anticipated, the effect of tunneling is significant in both models, and it must be included in the calculation. The KIEs computed from the two SRP models with tunneling included agree with each other within 23% at 300 K and within 12% for temperatures higher than 367.8 K.

To assess the extent of corner cutting in the tunneling, we compare the KIE factors calculated using the μ OMT method to those calculated using the ZCT method, which is appropriate for the zero-reaction-path curvature cases, in Table IX. The ZCT method accounts for about only 11–14% of the transmission probability estimated by the accurate method for the H-transfer reaction at 300K. Furthermore the contribution from tunneling to the KIE at 300 K is underestimated by a factor of two if only the tunneling processes along the MEP are considered. Therefore, a reasonable semiclassical approach should include corner cutting. From the canonical optimized multidimensional tunneling calculations, we found that the LCT-type tunneling dominates at low temperatures ($T < 350$ K in the SRP-1 model, and $T \leq 350$ K in the SRP-2 model) for the deuterium-transfer reaction, while SCT tunneling is more significant at high temperatures. For the hydrogen-transfer reaction, the tunneling is better represented by the large-curvature limit than the small-curvature one over the entire temperature range in the present study. In the following we only discuss the large-curvature results in detail to get a better understanding of the multidimensional tunneling process. We discuss only the SRP-2 calculations since the general nature of the tunneling process is found to be very similar for the two parameterizations.

Figure 7 shows the vibrationally adiabatic ground-state potential curves for the H-transfer reaction. In this figure we show $V_a^G(s)$ with respect to its value at $s = -\infty$, this is called $\Delta V_a^G(s)$ and is given by

$$\Delta V_a^G(s) = V_{\text{MEP}}(s) + \frac{1}{2} \hbar \sum_{m=1}^{3N-7} [\omega_m(s) - \omega_m(s = -\infty)] \quad (18)$$

since we define $V_{\text{MEP}}(s = -\infty)$ as the overall zero of energy. The horizontal lines indicate the so called⁸⁷ representative tunneling energies, which are the energies at which the integrand of the numerator of Eq. (11) has a maximum due to the compromise between the Boltzmann factor that decreases with energy and the tunneling probability that increases with energy; these representative tunneling energies are shown for 300, 367.8, and 1000 K. At any given energy, there are two points, s_ℓ and s_r , on the reaction path at which the energy equals the adiabatic ground-state energies $V_a^G(s_\ell)$ and $V_a^G(s_r)$. At the representative tunneling energy for a given temperature, the straight line between these points in the mass-scaled coordinates is called⁸⁷ the representative large-curvature tunneling path, and it can be viewed as defining the straight line along which a typical tunneling process occurs at that temperature. The angle between the imaginary normal mode eigenvector at the saddle point and the gradient on the MEP at each s is also plotted in Figure 7. The figure shows that the MEP curves by about 147° (72° on the reactant side and 75° on the product side) in mass-scaled coordinates over the classically forbidden region for the representative tunneling energy corresponding to 367.8 K. This illustrates the large-curvature nature of this reaction.

The highest accessible quasidiabatic excited state of the product has $n_p = 2$ for both H-transfer and D-transfer reactions with the SRP-1 parameterization, and it has $n_p = 3$ with the SRP-2 parameterization. (Recall that the quasidiabatic states are local wave packets representing the system instantaneously at the end of the tunneling part of the reactive traversal of the barrier region.⁴³) However the contributions from tunneling into excited states are very small, and for both the H- and D-transfer reactions the rate constants calculated including tunneling into excited states turned out to be within 1% of those that include ground state only.

To visualize the dynamics of this reaction, which has 21 internal degrees of freedom, we may picture it as a pseudo atom-diatom reaction, i.e., H and two "atoms", CF₃ and CD₃ in the case of the H-transfer reaction. The Jacobian coordinates of the pseudo triatomics are the distance of H to the center of mass of CD₃ and the distance of the center of mass of CF₃ to the center of mass of CD₃. A representation in mass-scaled (or mass-weighted) Jacobian coordinates provides a physically meaningful picture,⁷⁶ because the reduced mass along each degree of freedom is the same, and an N-particle problem in 3 dimensions becomes a one-particle problem in 3N dimensions. Figure 8 is based on the mass-scaled pseudo-Jacobian coordinates for the H-transfer reaction, and it shows the saddle point, the location of the CVT transition state for T = 367.8 K, and the representative large-curvature tunneling paths for tunneling into the ground state and the first excited state (i.e., $n_p = 1$) of the product side in the exoergic direction; the two representative tunneling paths correspond to the representative tunneling energy at 367.8 K. The asymptotes of the MEP in the figure define an angle which is 14°. This angle is called the skew angle β and can be calculated by^{34,88}

$$\tan^2 \beta = \frac{m_B(m_A + m_B + m_C)}{m_A m_C}, \quad (19)$$

for any reaction, A + BC → AB + C, where A, B, and C may be atoms or groups. Using Eq. (19), the skew angle is estimated to be 15° for the H-transfer reaction. The agreement in the skew angle estimated from Figure 8 and by using Eq. (19) indicates that the representation of the MEP in the mass-scaled pseudo-Jacobian coordinates is reasonable. The skew angle correlates to the curvature of the MEP because it is the supplement of the sum of the $s = -\infty$ and $s = +\infty$ limits of the dashed curve in Figure 7. The MEP of the H-transfer reaction has a smaller skew angle than the MEP of the D-transfer reaction, and the former has a larger curvature than the later.

The tunneling path for tunneling into the first excited state is much longer than the one for tunneling into the ground state. Combining this fact with the energetic factor provides qualitative explanation for the negligible contribution from tunneling into excited states for these particular reactions.

In Figure 8, we labeled the classical turning points [see Eq. (14)] of the representative large-curvature tunneling path for tunneling into the ground state at 367.8 K as s_a and s_b . Figure 8 shows that the representative large-curvature tunneling path is considerably shorter than the portion of the MEP from s_a to s_b . Figure 9 presents the Born-Oppenheimer potential along the representative large-curvature tunneling path and along the MEP from s_a to s_b ; the latter quantity is $V_{\text{MEP}}(s)$. The maximum of the Born-Oppenheimer potential along the representative large-curvature tunneling path is higher than the Born-Oppenheimer barrier along the MEP (which is, of course, the reaction path with the smallest possible barrier). Since the representative large-curvature tunneling path is shorter, the barrier along the representative large-curvature tunneling path is much thinner than the barrier along the MEP. Figure 10 presents the effective potential barrier⁴³ for large-curvature tunneling along the representative large-curvature tunneling path and the effective potential, $V_a^G(s)$, along the MEP. Figure 10 shows that the effective tunneling barrier along the representative large-curvature tunneling path is much thinner than the effective tunneling barrier along the MEP, and this evidence supports the preference of the large-curvature tunneling path over the MEP, since, semiclassically, the nature of the tunneling process is determined by the length of the tunneling path and the effective potential along that tunneling path.^{55,72} For reference we note that the calculated tunneling probabilities using the ZCT, SCT, and LCT methods are 6.2×10^{-4} , 5.2×10^{-3} , and 2.3×10^{-2} , for the H-transfer reaction in the SRP-2 model at the representative tunneling energy for the LCT calculation at 367.8 K.

Figure 8 shows that the representative large-curvature tunneling path is almost parallel to the H-CD₃ axis. This indicates the nature of the tunneling process in a

semiclassical sense. Table V gives the geometries of the generalized transition state at s_a to s_b , and it shows that tunneling involves mainly the motion of the migrating H, although the C-C distance decreases by 0.08 Å.

We note that the experimental rate constants may have large errors. If the true barrier is lower than estimated here, tunneling may be correspondingly less important.

V. Concluding Remarks

We have shown that the NDDO-SRP approach provides convenient and reasonable force fields for the prototype reactions in the present study. (This is a severe test for this approach since F is a particularly difficult atom for the AM1 method to treat accurately.) In the present study we use the NDDO-SRP approach to model the force field not only at the conventional transition state and along the whole reaction path but also throughout the reaction swath, which is defined^{1,2,15} as the region, wider than the valley that can be described in a curvilinear coordinate system including the minimum-energy-path reaction progress variable, that is required to describe corner-cutting dynamics when reaction-path curve is large. Our results also indicate that conclusions drawn from different SRP models obtained by fitting the same set of properties are very similar, and therefore the understanding of the dynamics is not sensitive to the choices of which parameters are adjusted, provided that the adjustment is small. Our results also show that the SRP models obtained by fitting to a specific isotopic reaction may be used for predictions of the kinetic isotope effect. Thus the present results indicate that the NDDO-approach can provide realistic generalized transition state force fields for chemical reactions, and the detailed modeling of more complex organic and biochemical reactions is be a reasonable goal for this method in the near future.

The calculations are equally important for showing the accuracy that can be attained for the dynamics by the optimized multidimensional tunneling approximation for a system with large reaction-path curvature. We note in this regard that all bimolecular hydrogen-

atom, hydride, and proton transfer reactions have large reaction-path curvature. We conclude that variational transition state theory and multidimensional semiclassical tunneling calculations including corner cutting, combined with the NDDO-SRP technique, provides a powerful method for modeling and understanding the detailed quantum mechanical dynamics of organic reactions.

Acknowledgments

The authors are grateful to Gillian C. Lynch for collaboration on the LCG3 option in the POLYRATE program. This work was supported in part by the U.S. Department of Energy through a grant from the Division of Chemical Sciences, Office of Basic Energy Sciences, Office of Energy Research by a grant to D. G. T., and under contract DE-AC06-78RLO 1830 with Battelle Memorial Institute which operates the Pacific Northwest Laboratory.

Literature cited

1. Truhlar, D. G.; Brown, F. B.; Steckler, R.; Isaacson, A. D. In *The Theory of Chemical Reaction Dynamics*; Clary, D. C., Ed.; NATO ASI Series C170; Reidel: Dordrecht, Holland, 1986; pp 286–329.
2. Truhlar, D. G.; Steckler, R.; Gordon, M. S. *Chem. Rev.* 1987, 87, 217. The first half of this reference reviews global potential energy functions for relative systems, and the second half reviews ab initio electronic structure calculations applied to map out potentials along a dynamical path.
3. Schatz, G. C. *Rev. Mod. Phys.* 1989, 61, 669.
4. (a) Wang, I.; Karplus, M. *J. Amer. Chem. Soc.* 1973, 95, 8160. (b) Warshel, A.; Karplus, M. *Chem. Phys. Lett.* 1975, 32, 11.
5. Malcome-Lawes, D. J. *J. Chem. Soc. Faraday Trans. 2* 1975, 71, 1183.
6. Morokuma, K.; Kato, S. In *Potential Energy Surfaces and Dynamics Calculations*, Plenum: New York, 1981; pp. 243–264.
7. Gray, S. K.; Miller, W. H.; Yamaguchi, Y.; Schaefer, H. F. *J. Amer. Chem. Soc.* 1981, 103, 1900.
8. Truhlar, D. G.; Duff, J. W.; Blais, N. C.; Tully, J. C.; Garrett, B. C. *J. Chem. Phys.* 1982, 77, 764.
9. Colwell, S. M.; Handy, N. C. *J. Chem. Phys.* 1985, 82, 1281.
10. Car, R.; Parrinello, M. *Phys. Rev. Lett.* 1985, 55, 2471.
11. (a) Tachibana, A.; Okazaki, I.; Koizumi, M.; Hori, K.; Yamabe, T. *J. Amer. Chem. Soc.* 1985, 107, 1190. (b) Tachibana, A.; Fueno, H.; Yamabe, T. *J. Amer. Chem. Soc.* 1986, 108, 4346.
12. Doubleday, C., Jr.; McIver, J. W., Jr.; Page, M. *J. Phys. Chem.* 1988, 92, 4367.
13. Baldridge, K. K.; Gordon, M. S.; Steckler, R.; Truhlar, D. G. *J. Phys. Chem.* 1989, 93, 5107.

14. Car, R.; Parrinello, M. In *Simple Molecular Systems at Very High Density*; Polian, A., Loubeyre, P.; Bocvara, N., Eds.; Plenum: New York, 1989; p. 455.
15. Truhlar, D. G.; Gordon, M. S. *Science* **1990**, *249*, 491.
16. Remler, D.; Madden, P.A. *Mol. Phys.* **1990**, *70*, 921.
17. Garrett, B. C.; Koszykowski, M. L.; Melius, C. F.; Page, M. *J. Phys. Chem.* **1990**, *94*, 7096.
18. Field, M. *J. Chem. Phys. Lett.* **1990**, *172*, 83.
19. Helgaker, T.; Uggerud, E.; Jensen, H. J. A. *Chem. Phys. Lett.* **1990**, *173*, 145.
20. Gonzalez-Lafont, A.; Truong, T. N.; Truhlar, D. G. *J. Phys. Chem.* **1991**, *95*, 4618.
21. Truong, T. N.; McCammon, J. A. *J. Amer. Chem. Soc.* **1991**, *113*, 7504.
22. Viggiano, A. A.; Paschkewitz, J.; Morris, R. A.; Paulson, J. F.; Gonzalez-Lafont, A.; Truhlar, D. G. *J. Amer. Chem. Soc.* **1991**, *113*, 9404.
23. Garrett, B. C.; Melius, C. F.; Page, M. In *Theoretical and Computational Models for Organic Chemistry*; Formosinho, S. J., Csizmadia, I. G., Arnaut, L. G., Eds.; Kluwer: Dordrecht, 1991; pp 35–54.
24. Uggerud, E.; Helgaker, T. *J. Amer. Chem. Soc.* **1992**, *114*, 4265.
25. Hartke, B.; Carter, E. A. *J. Chem. Phys.* **1992**, *97*, 6569.
26. Liu, Y.-P.; Lynch, G. C.; Truong, T. N.; Lu, D.-h.; Truhlar, D. G. *J. Amer. Chem. Soc.* **1993**, *115*, 2408.
27. Pople, J. A.; Santry, D. P.; Segal, G. A. *J. Chem. Phys.* **1965**, *43*, S129.
28. Dewar, M. J. S.; Thiel, W. *J. Amer. Chem. Soc.* **1977**, *99*, 4899.
29. Dewar, M. J. S.; Zoebisch, E. G.; Healy, E. F.; Stewart, J. J. P. *J. Amer. Chem. Soc.* **1985**, *107*, 3902. Dewar, M. J. S.; Zoebisch, E. G. *J. Mol. Struct. (Theochem)* **1988**, *180*, 1.
30. Stewart, J. J. P. *J. Comput. Chem.* **1989**, *10*, 209. Stewart, J. J. P. *J. Computer-Aided Molecular Design* **1990**, *4*, 48.

31. Garrett, B. C.; Truhlar, D. G. *J. Chem. Phys.* **1979**, *70*, 1593.
32. Truhlar, D. G.; Garrett, B. C. *Accounts Chem. Res.* **1980**, *13*, 440.
33. Truhlar, D. G.; Isaacson, A. D.; Skodje, R. T.; Garrett, B. C. *J. Phys. Chem.* **1982**, *86*, 2252.
34. Truhlar, D. G.; Isaacson, A. D.; Garrett, B. C. In *Theory of Chemical Reaction Dynamics*; Baer, M., Ed; CRC Press: Boca Raton, Florida, 1985; Vol. 4, pp 65–137.
35. Truhlar, D. G.; Garrett, B. C. *Annu. Rev. Phys. Chem.* **1984**, *35*, 159.
36. Truhlar, D. G.; Garrett, B. C. *J. Chim. Phys.* **1987**, *84*, 365.
37. Tucker, S. C.; Truhlar, D. G. In *New Theoretical Concepts for Understanding Organic Reactions*; Bertran, J.; Csizmadia, I. G., Eds.; NATO ASI Series C267; Kluwer: Dordrecht, Netherlands, 1989; pp 291–346.
38. For early work on variational transition state theory, see: (a) Wigner, E. *J. Chem. Phys.* **1937**, *5*, 720. (b) Horiuti, J. *Bull. Chem. Soc. Jpn.* **1938**, *13*, 210. (c) Keck, J. C. *J. Chem. Phys.* **1960**, *32*, 1035. (d) Keck, J. C. *Adv. Chem. Phys.* **1967**, *13*, 85. (e) Eliason, M. A.; Hirschfelder, J. O. *J. Chem. Phys.* **1959**, *30*, 1426.
39. See also: (a) Quack, M.; Troe, J. *Bunsenges. Physik. Chem.* **1977**, *81*, 329. (b) Quack, M.; Troe, J. *Chem. Soc. Specialist Periodical Report Gas Kinetics and Energy Transfer* **1977**, *2*, 175. (c) Pechukas, P. *Annu. Rev. Phys. Chem.* **1981**, *32*, 159. (d) Chesnavich, W. J.; Bowers, M. T. *Progress Reaction Kinetics* **1982**, *11*, 137. (e) Martin, D. L.; Raff, L. M. *J. Chem. Phys.* **1982**, *77*, 1235. (f) Hase, W. L. *Accounts Chem. Res.* **1983**, *16*, 258. (g) Chesnavich, W. J. *J. Chem. Phys.* **1986**, *84*, 2615. (h) Laidler, K. J. *Chemical Kinetics*, 3rd edition, Harper & Row: New York, 1987. (i) Klippenstein, S. J.; Marcus, R. A. *J. Chem. Phys.* **1987**, *87*, 3410. (j) Sverdlik, D. I.; Koeppl, G. W. *J. Chem. Phys.* **1989**, *91*, 250. (k) Schranz, H. W.; Raff, L. M.; Thompson, D. L. *Chem. Phys. Lett.* **1990**, *171*, 68.

40. Garrett, B. C.; Truhlar, D. G.; Wagner, A. F.; Dunning, T. H., Jr. *J. Chem. Phys.* **1983**, *78*, 4400.
41. Garrett, B. C.; Abusalbi, N.; Kouri, D. J.; Truhlar, D. G. *J. Chem. Phys.* **1985**, *83*, 2252.
42. Kreevoy, M. M.; Ostovic, D.; Truhlar, D. G.; Garrett, B. C. *J. Phys. Chem.* **1986**, *90*, 3766.
43. Lu, D.-h.; Truong, T. N.; Melissas, V.; Lynch, G. C.; Liu, Y.-P.; Garrett, B. C.; Steckler, R.; Isaacson, A. D.; Rai, S. N.; Hancock, G. C.; Lauderdale, J. G.; Joseph, T.; Truhlar, D. G. *Computer Phys. Commun.* **1992**, *71*, 235.
44. Garrett, B. C.; Joseph, T.; Truong, T. N.; Truhlar, D. G. *Chem. Phys.* **1989**, *136*, 271.
45. Truong, T. N.; Lu, D.-h.; Lynch, G. C.; Liu, Y.-P.; Melissas, V. S.; Stewart, J. J. P.; Steckler, R.; Garrett, B. C.; Isaacson, A. D.; Gonzalez-Lafont, A.; Rai, N. N.; Hancock, G. C.; Joseph, T.; Truhlar, D. G. *Computer Phys. Commun.* **1993**, *75*, 143.
46. Ayscough, P. B.; Polanyi, J. C.; Steacie, E. W. R. *Can. J. Chem.* **1955**, *33*, 743.
47. Sharp, T. E.; Johnston, H. S. *J. Chem. Phys.* **1962**, *37*, 1541.
48. Carmichael, H.; Johnston, H. S. *J. Chem. Phys.* **1964**, *41*, 1975.
49. Alcock, W. G.; Whittle, E. *Trans. Faraday Soc.* **1965**, *61*, 244.
50. Giles, R. D.; Quick, L. M.; Whittel, E. *Trans. Faraday Soc.* **1967**, *63*, 662.
51. Arican, H. M.; Potter, E.; Whytock, D. A. *J. Chem. Soc., Faraday Trans. I*, **1973**, *69*, 1811.
52. Arican, H.; Arthur, N. L. *Int. J. Chem. Kinet.* **1986**, *18*, 437.
53. Lane, S. I.; Oexler, E. V.; Staricco, E. H. *Int. J. Chem. Kinet.* **1991**, *23*, 361.
54. Gray, P.; Herod, A. A.; Jones, A. *Chem. Rev.* **1971**, *71*, 247.
55. Garrett, B. C.; Truhlar, D. G. *J. Chem. Phys.* **1983**, *79*, 4931.
56. Pitzer, K. S.; Gwinn, W. D. *J. Chem. Phys.* **1942**, *10*, 428.

57. Truhlar, D. G. *J. Comput. Chem.* **1991**, *12*, 266.
58. Parr, C. A.; Truhlar, D. G. *J. Phys. Chem.* **1971**, *75*, 1844.
59. Brown, S. B.; Dewar, M. J. S.; Ford, F. P.; Nelson, D. J.; Rzepa, H. S. *J. Amer. Chem. Soc.* **1978**, *100*, 7832.
60. Dewar, M. J. S.; Thiel, W. *Theoret. Chim. Acta* **1977**, *46*, 89.
61. Pople, J. A.; Nesbet, R. K. *J. Chem. Phys.* **1954**, *22*, 571.
62. Shavitt, I. *Theoretical Chemistry Laboratory Report No. WIS-AEC-23*, University of Wisconsin, Madison, 1959.
63. Marcus, R. A. *J. Chem. Phys.* **1964**, *41*, 610.
64. Marcus, R. A. *J. Chem. Phys.* **1966**, *45*, 4493.
65. Truhlar, D. G.; Kuppermann, A. *J. Amer. Chem. Soc.* **1971**, *93*, 1840.
66. Fukui, K. In *The World of Quantum Chemistry*; Daudel, R.; Pullman, B., Eds.; Reidel: Dordrecht, Holland, 1974; pp 113–141. Fukui, K. In *Applied Quantum Chemistry*, Smith, V. H., Jr., Schaefer, H. F. III, Morokuma, K., Eds.; Reidel: Dordrecht, 1986; pp 1–25.
67. Miller, W. H.; Handy, N. C.; Adams, J. E. *J. Chem. Phys.* **1980**, *72*, 99.
68. Natanson, G. A.; Garrett, B. C.; Truong, T. N.; Joseph, T.; Truhlar, D. G. *J. Chem. Phys.* **1991**, *94*, 7875.
69. Davidson, N. *Statistical Mechanics*; McGraw-Hill: New York, 1962; pp 194–202.
70. Garrett, B. C.; Truhlar, D. G.; Grev, R. S.; Magnuson, A. W. *J. Phys. Chem.* **1980**, *84*, 1730.
71. Marcus, R. A.; Coltrin, M. E. *J. Chem. Phys.* **1977**, *67*, 2609.
72. Skodje, R. T.; Truhlar, D. G.; Garrett, B. C. *J. Chem. Phys.* **1982**, *77*, 5955.
73. Truhlar, D. G.; Lu, D.-h.; Tucker, S. C.; Zhao, X. G.; Gonzalez-Lafont, A.; Truong, T. N.; Maurice, D.; Liu, Y.-P.; Lynch, G. C. In *Isotope Effects in Gas-Phase Chemistry*, Kaye, J. A., Ed.; American Chemical Society, Washington, 1992; pp 16–36.

74. Garrett, B. C.; Truhlar, D. G. *J. Phys. Chem.* **1979**, *83*, 2921.
75. Eyring, H. *J. Chem. Phys.* **1935**, *3*, 107.
76. Glasstone, S.; Laidler, K. J.; Eyring, H. *Theory of Chemical Rate Processes*, McGraw-Hill: New York, 1941.
77. Pollak, E.; Pechukas, P. *J. Amer. Chem. Soc.* **1978**, *100*, 2984.
78. Coulson, D. R. *J. Amer. Chem. Soc.* **1978**, *100*, 2992.
79. Ishida, K.; Morokuma, K.; Komornicki, A. *J. Chem. Phys.* **1977**, *66*, 2153.
80. Schmidt, M. W.; Gordon, M. S.; Dupuis, M. *J. Amer. Chem. Soc.* **1985**, *107*, 2585.
81. Garrett, B. C.; Redmon, M. J.; Steckler, R.; Truhlar, D. G.; Baldridge, K. K.; Bartol, D.; Schmidt, M. W.; Gordon, M. S. *J. Phys. Chem.* **1988**, *92*, 1476
82. Isaacson, A. D.; Truhlar, D. G.; Rai, S. N.; Steckler, R.; Hancock, G. C.; Garrett, B. C.; Redmon, M. J. *Computer Phys. Commun.* **1987**, *47*, 91.
83. Solamoglu, N.; Rossi, M. J.; Golden, D. M. *Chem. Phys. Lett.* **1986**, *124*, 68.
84. Glanzer, K.; Maier, M.; Troe, J. *J. Phys. Chem.* **1980**, *84*, 1681.
85. Chase, M. W.; Davies, C. A.; Downey, J. R.; Frurip, D. R.; McDonald, R. A.; Syverud, A. N. *JANAF Thermochemical Tables*, 3rd Ed., 1985 Supplement, *J. Phys. Chem. Ref. Data.* **1985**, *14*, Suppl. 1.
86. Lu, D.-h.; Maurice, D.; Truhlar, D. G. *J. Amer. Chem. Soc.* **1990**, *112*, 6206.
87. Kim, Y.; Truhlar, D. G.; Kreevoy, M. M. *J. Amer. Chem. Soc.* **1991**, *113*, 7837.
88. Mahan, B. H. *J. Chem. Educ.* **1974**, *51*, 309.

Table I. SRP-1 and SRP-2 parameters

Atom	Parameter	AM1	SRP-1	SRP-2
C	ζ_s	1.808665	1.861999	— ^a
C	ζ_p	1.685116	1.710448	1.735563
C	β_s	-15.715783	-16.534404	-16.286762
H	ζ_s	1.188078	1.274984	1.250107
H	β_s	-6.173787	-5.653369	-5.653369
H	U_{ss}	-11.396427	— ^a	-11.774451
F	ζ_s	2.494670	2.703716	2.703716

^aSame as the AM1 parameters.

Table II. Harmonic vibrational normal mode frequencies(in cm^{-1}) of CH_4 , CF_3 , CH_3 , and CF_3H from experiment and from AM1 and the two SRP models

	Expt. ^a	AM1	SRP-1	SRP-2
CH_4				
	3019	3216	3230	3219
	3019	3104	3099	3095
	3019	3104	3099	3095
	2917	3104	3099	3095
	1534	1412	1436	1428
	1534	1412	1436	1428
	1306	1380	1408	1404
	1306	1380	1408	1404
	1306	1380	1408	1404
CF_3				
	1259	1590	1488	1488
	1259	1591	1488	1488
	1090	1145	1118	1111
	701	483	570	565
	500	430	412	411
	500	430	417	414
CH_3				
	3184	3250	3259	3257
	3184	3252	3276	3268
	3002	3250	3259	3257
	1383	1348	1371	1365
	1383	1348	1371	1365
	580	780	790	767
CF_3H				
	3035	3003	3055	3067
	1376	1501	1423	1429
	1376	1504	1423	1429
	1152	1316	1279	1275
	1152	1234	1222	1220
	1137	1232	1222	1220
	700	610	596	593
	508	432	425	424
	508	429	424	423

^aFrom Ref. 84.

Table III. Properties from experiment and from calculations with the AM1, SRP-1, and SRP-2 Hamiltonians

	ΔE^a (kcal/mol)	bond energy		frequencies	
		CH ₃ -H	CF ₃ -H	RMS ^b	max $\Delta\omega^c$
experiment ^d	-0.72	112.18	112.90		
AM1	10.65	90.85	80.20	137	332
SRP-1	-0.24	80.05	80.29	122	257
SRP-2	-0.75	80.51	81.25	120	255

^a ΔE is the energy of reaction.

^bRoot-mean-square of the deviation of calculated frequencies with respect to experimental frequencies.

^cMaximum deviation.

^dEstimated from the heat of formation at 0 K and the vibrational frequencies, which are from Ref. 84.

Table IV. Bond lengths in Å

molecule	CH_4	CF_4	CH_3	CF_3H	CF_3H
bond	CH	CF	CH	CH	CF
experiment ^a	1.09	1.33	1.08	1.10	1.33
AM1	1.11	1.33	1.09	1.13	1.37
SRP-1	1.10	1.32	1.07	1.11	1.36
SRP-2	1.11	1.32	1.08	1.11	1.36

^aFrom Ref. 84.

Table V. Geometry of the saddle point and termini of the representative large-curvature tunneling path at 367.8K for the H-transfer reaction^a

	R ₁ (Å)	R ₂ (Å)	R ₃ (Å)	R ₄ (Å)	α ₁ (deg)	α ₂ (deg)
saddle point						
AM1	1.39	1.27	1.10	1.36	102	112
SRP-1	1.32	1.30	1.09	1.35	104	112
SRP-2	1.33	1.31	1.09	1.35	104	112
tunneling path termini (SRP-2)						
s _a	1.11	1.62	1.10	1.34	106	111
s _b	1.50	1.15	1.08	1.36	97	113

^aSee Figure 1 for definitions of coordinates.

^blabeled as s_a and s_b in Figure 8.

Table VI. Vibrational normal mode frequencies (in cm^{-1}) of eclipsed C_{3v} conformation of $\text{CF}_3-\text{H}-\text{CH}_3$ in the two SRP models

AM1 ^a	SRP-1	SRP-2
3203	3210	3207
3171	3157	3159
3171	3157	3159
1510	1426	1428
1510	1426	1428
1369	1386	1381
1359	1386	1381
1358	1380	1370
1275	1249	1247
1218	1245	1247
1218	1245	1245
664	653	650
597	588	587
597	588	587
455	415	414
425	413	413
424	410	409
94	93	100
90	91	96
... ^b	24	22

^aCalculated by taking the central difference of the gradients from program MOPAC with a stepsize of 0.012 $\text{a}\text{\AA}$.

^bThe lowest frequency mode in the AM1 hamiltonian is not stable with respect to the numerical stepsize with available computer programs. The eigenvector of this mode indicates that it corresponds to internal rotation about the C_3 axis, and the potential energy profile obtained by rotating the methyl group with respect to the trifluoromethyl group with all other degrees of freedom optimized shows the eclipsed conformation is the minimum of internal rotation.

Table VII. Reaction rate constants ($\text{cm}^3 \text{molecule}^{-1} \text{s}^{-1}$) at 626.8 K

	k_{H}^{a}	k_{D}^{b}	KIE ^c
TST			
SRP-1	1.3×10^{-17}	1.8×10^{-17}	2.1
SRP-2	1.3×10^{-17}	1.8×10^{-17}	2.1
CVT			
SRP-1	1.0×10^{-17}	1.5×10^{-17}	2.1
SRP-2	1.0×10^{-17}	1.5×10^{-17}	2.1
CVT/μOMT			
SRP-1	2.6×10^{-17}	2.6×10^{-17}	3.0
SRP2	2.7×10^{-17}	2.7×10^{-17}	3.0
experimental^d			
	2.8×10^{-17}	2.6×10^{-17}	3.2

^a k_{H} is the rate constant of the reaction $\text{CF}_3 + \text{CD}_3\text{H} \rightarrow \text{CF}_3\text{H} + \text{CD}_3$.

^b k_{D} is the rate constant of the reaction $\text{CF}_3 + \text{CD}_3\text{H} \rightarrow \text{CF}_3\text{D} + \text{CD}_2\text{H}$.

^cKIE is defined as the ratio of k_{H} to $\frac{1}{3}k_{\text{D}}$, which is the rate constant for transferring a single deuterium atom.

^dExperimental results are from Ref. 47.

Table VIII. Tunneling transmission coefficients and factorized KIEs

T	$k_H^{CVT/\mu OMT}(T)$	$k_H^{CVT/\mu OMT}$	$\frac{k_H^{CVT/\mu OMT}(T)}{k_D^{CVT/\mu OMT}(T)}$	$\frac{k_H^{CVT}(T)}{k_D^{CVT}(T)}$	$\frac{k_H^{CVT/\mu OMT}(T)}{k_D^{CVT/\mu OMT}(T)}$
SRP-1					
300	6.7×10^1	4.3×10^{-21}	2.4	5.4	13
367.8	1.7×10^1	6.3×10^{-20}	2.1	3.9	8.1
400	1.1×10^1	1.8×10^{-19}	1.9	3.5	6.7
600	2.8×10^0	1.7×10^{-17}	1.4	2.2	3.2
1000	1.4×10^0	1.7×10^{-15}	1.1	1.6	1.7
SRP-2					
300	8.1×10^1	6.0×10^{-21}	2.9	5.5	16
367.8	1.8×10^1	7.4×10^{-20}	2.3	4.0	9.1
400	1.1×10^1	2.0×10^{-19}	2.1	3.6	7.4
600	2.8×10^0	1.8×10^{-17}	1.4	2.3	3.3
1000	1.4×10^0	1.7×10^{-15}	1.1	1.6	1.7
Expt.^a					
367.8	$3.9 \begin{matrix} -1.3 \\ +2.0 \end{matrix} \times 10^{-20}$				11.8

^aExperimental results are from Ref. 47. Error bars are estimated from the error bar in the Arrhenius fit of the relative H-transfer reaction rate constants referenced to the recombination rate constants of the trifluoromethyl radical. The error in the recombination rate constants is not included.

Table IX. KIE factors calculated from the μ OMT transmission coefficients and from the ZCT transmission coefficients

T	$\kappa_H^{CVT/\mu\text{OMT}}(T)$	$\frac{\kappa_H^{CVT/\mu\text{OMT}}(T)}{\kappa_D^{CVT/\mu\text{OMT}}(T)}$	$\kappa_H^{CVT/ZCT}(T)$	$\frac{\kappa_H^{CVT/ZCT}(T)}{\kappa_D^{CVT/ZCT}(T)}$
SRP-1				
300	67	2.4	9.1	1.2
367.8	17	2.1	4.6	1.2
400	11	1.9	3.7	1.2
600	2.8	1.4	1.8	1.2
1000	1.4	1.1	1.2	1.0
SRP-2				
300	81	2.9	11	1.4
367.8	18	2.3	4.9	1.3
400	11	2.1	3.9	1.3
600	2.8	1.4	1.9	1.2
1000	1.4	1.1	1.2	1.0

Figure captions

- Figure 1.** Coordinates for describing the transition state. The structure actually shown is the SRP-2 saddle point.
- Figure 2.** The Born-Oppenheimer potential energy profile along the reaction path as a function of the reaction coordinate for the H-transfer reaction. The solid line represents SRP-1 model, and the dotted line represents the SRP-2 model.
- Figure 3.** The adiabatic ground-state potential energy profile along the reaction path as a function of the reaction coordinate for the H-transfer reaction. The solid line represents SRP-1 model, and the dotted line represents the SRP-2 model.
- Figure 4.** Logarithm to the base 10 of k_H in $\text{cm}^3 \text{ molecule}^{-1} \text{ s}^{-1}$ vs. the reciprocal of temperature.
- Figure 5.** Logarithm to the base 10 of $k_D/3$ in $\text{cm}^3 \text{ molecule}^{-1} \text{ s}^{-1}$ vs. the reciprocal of temperature.
- Figure 6** The kinetic isotope effect vs. the reciprocal of temperature. The experimental data are shown as circles; the curves are 7th order polynomial fits to the present calculations. The KIEs are computed as the ratio of the H-transfer rate constant to the rate constant of transferring a single deuterium atom.
- Figure 7.** Reaction path quantities as a function of the reaction coordinate for the H-transfer reaction calculated with the SRP-2 parameterization. The adiabatic potential energy curve with respect to the adiabatic potential of the reactants, $\Delta V_a^G(s)$, is shown as a solid curve, and the angle between the imaginary normal mode eigenvector and the gradient is shown as a dashed curve. The horizontal lines indicate the representative tunneling energies, and the thin vertical lines indicate the termini of the representative large-curvature tunneling path at the representative tunneling energy at 367.8 K.
- Figure 8.** Representative large-curvature tunneling paths and MEP in the mass-scaled pseudo-Jacobian coordinates, for the H-transfer reaction of the SRP-2 model. The two

representative large-curvature tunneling paths are for tunneling from the ground state to ground state (shorter path) and from the ground state to the first excited state (longer path) at 367.8 K.

- Figure 9.** The Born-Oppenheimer potential along the MEP and along the representative large-curvature tunneling path for tunneling from the ground state to the ground state for the H-transfer reaction in the SRP-2 model.
- Figure 10.** The effective potential along the MEP and along the representative large-curvature tunneling path for tunneling from the ground state to the ground state for the H-transfer reaction in the SRP-2 model.

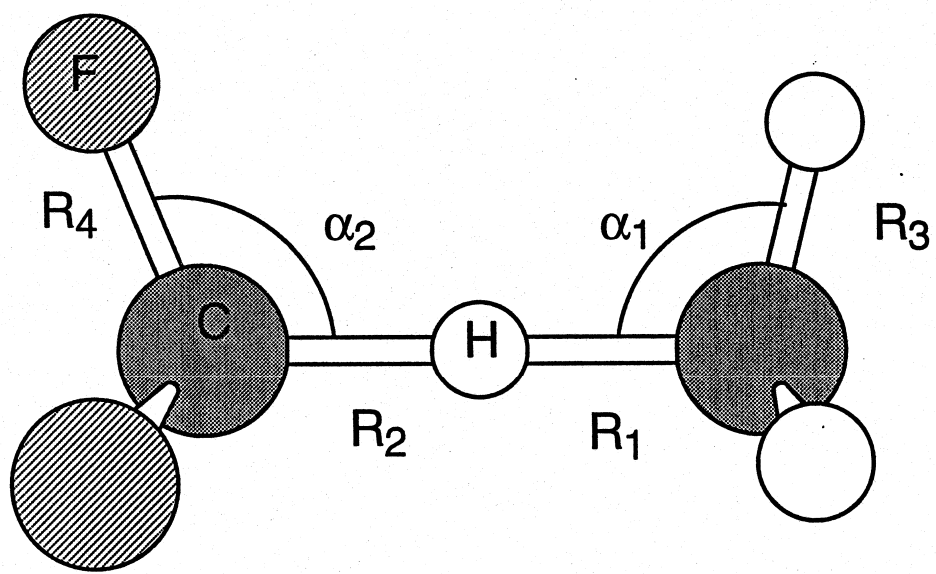


Figure 1

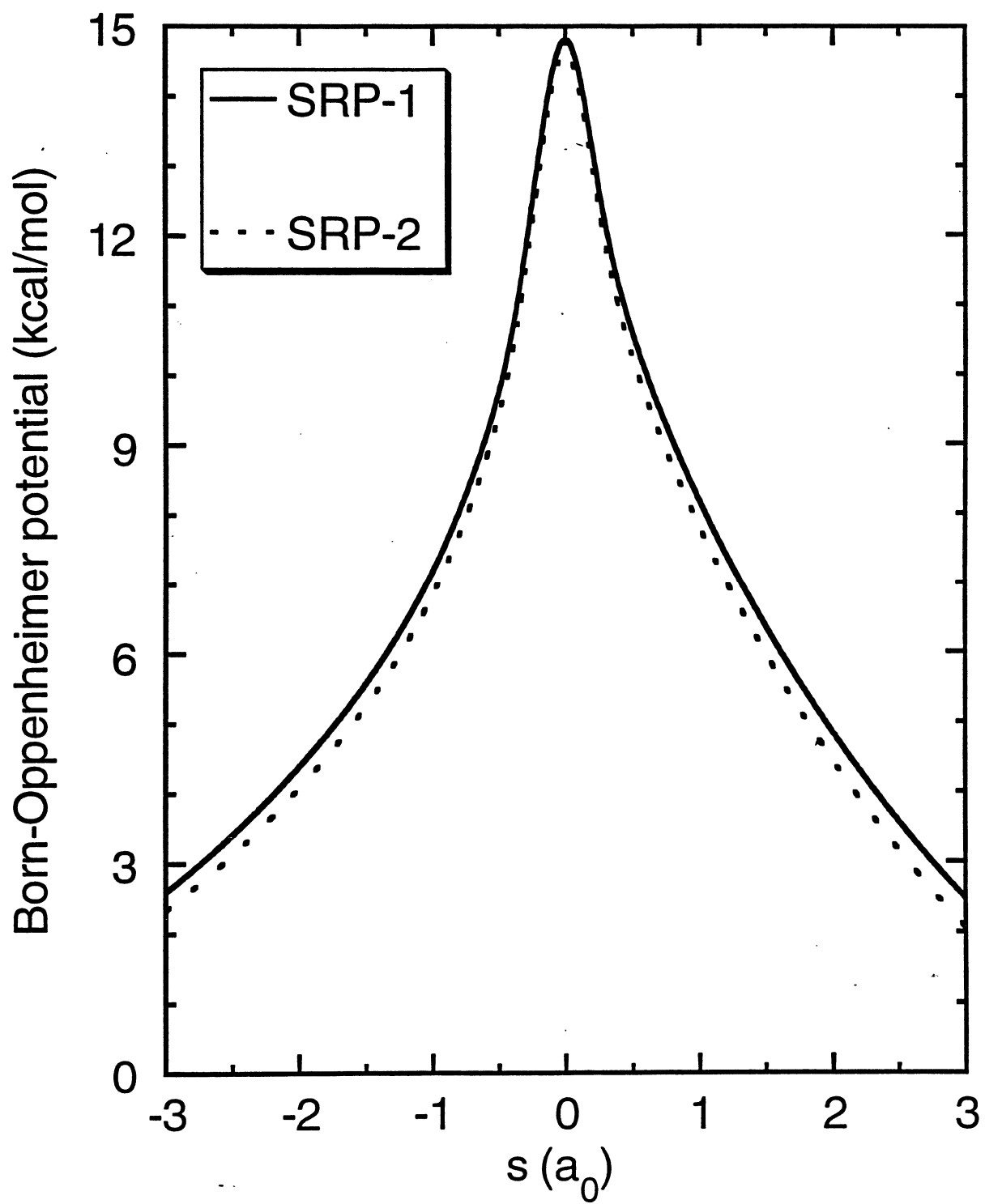


Figure 2

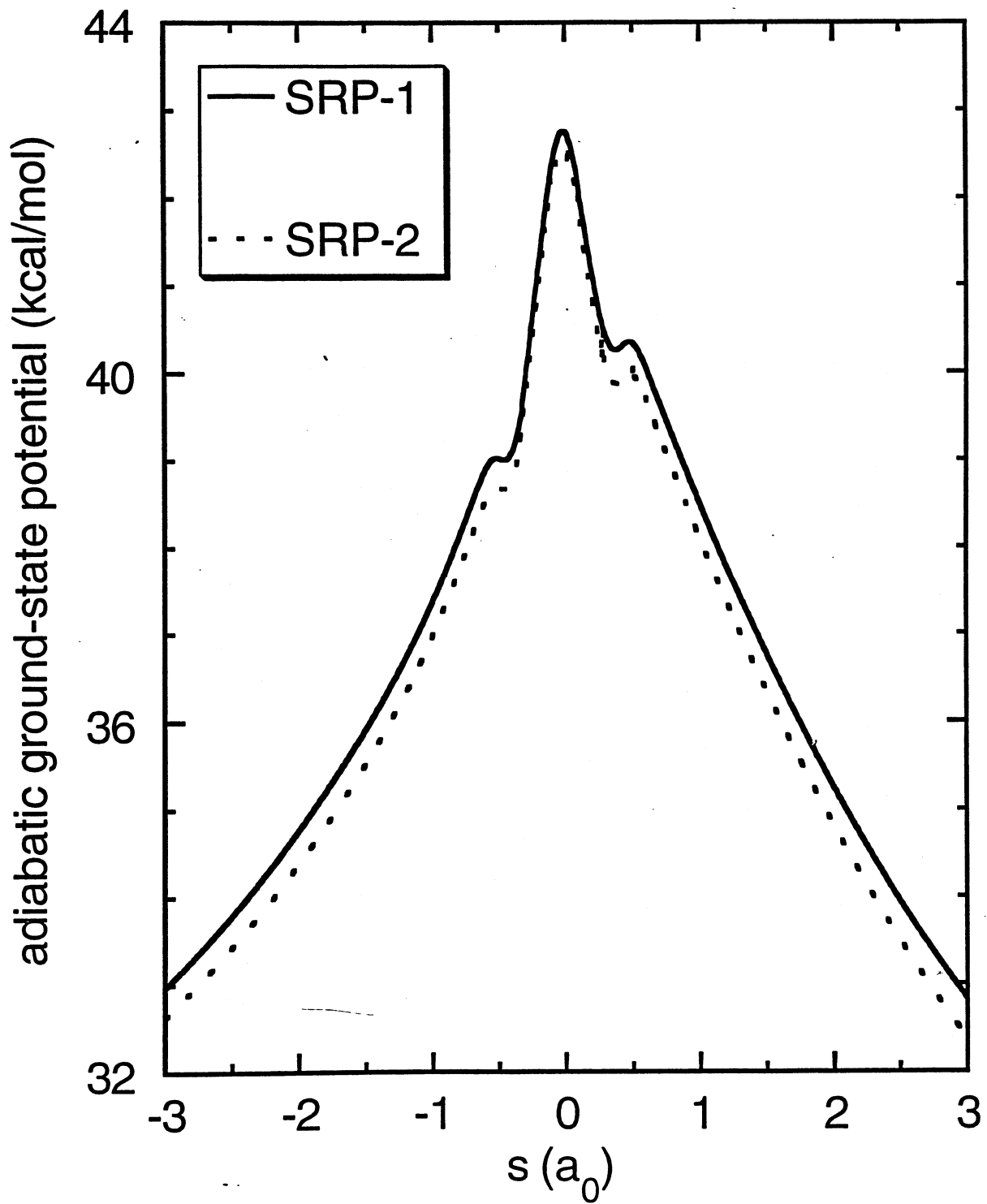


Figure 3

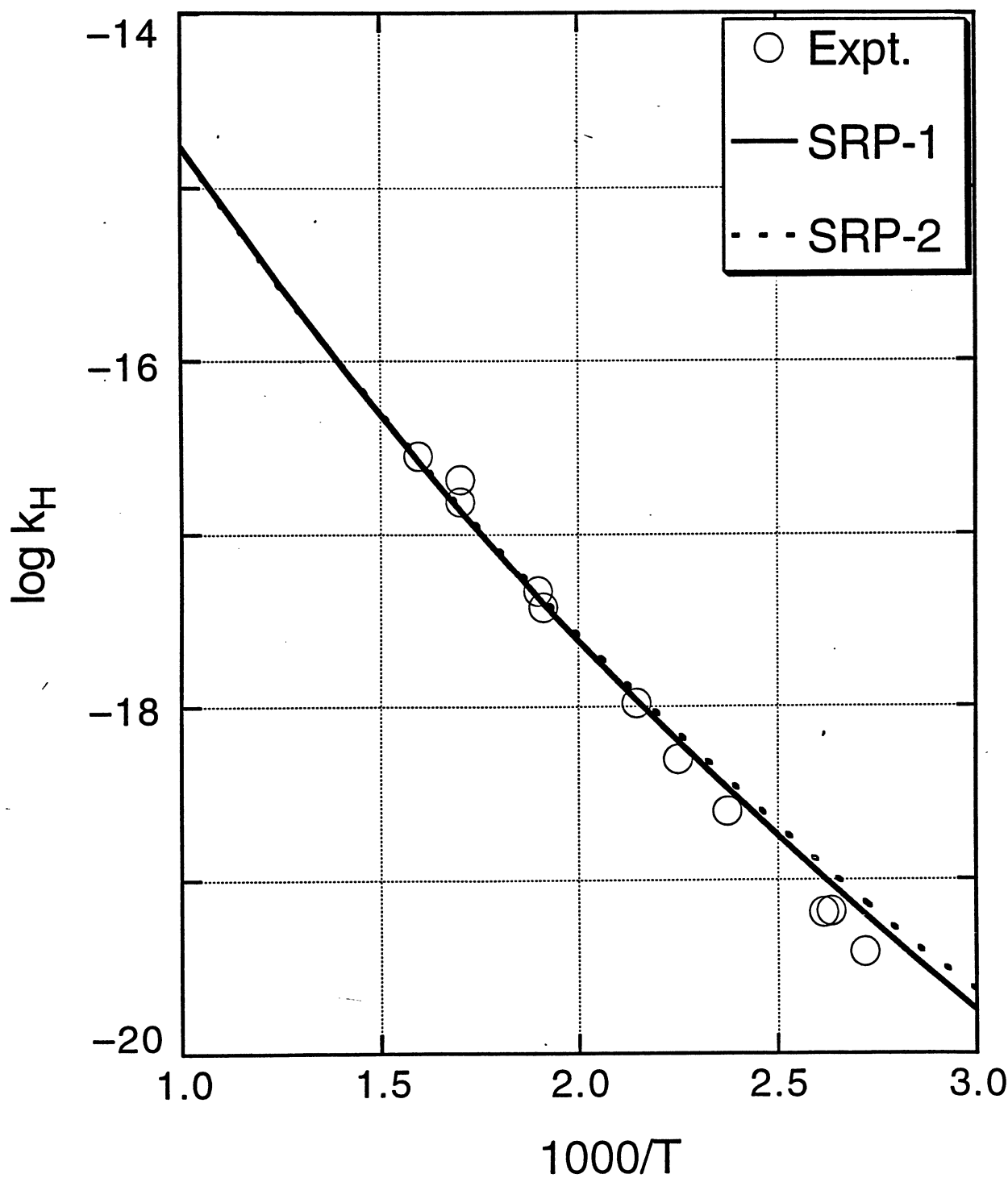


Figure 4

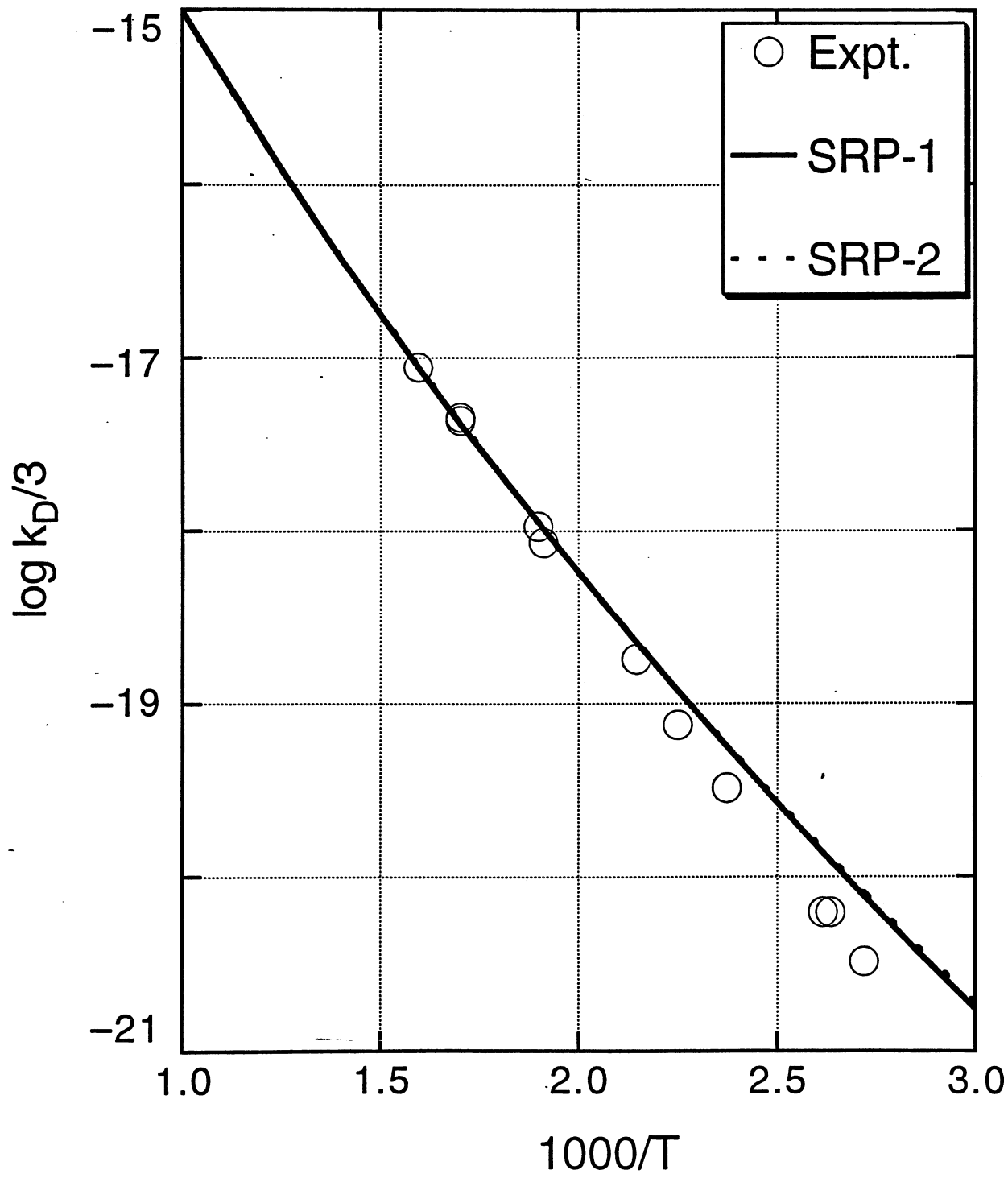


Figure 5

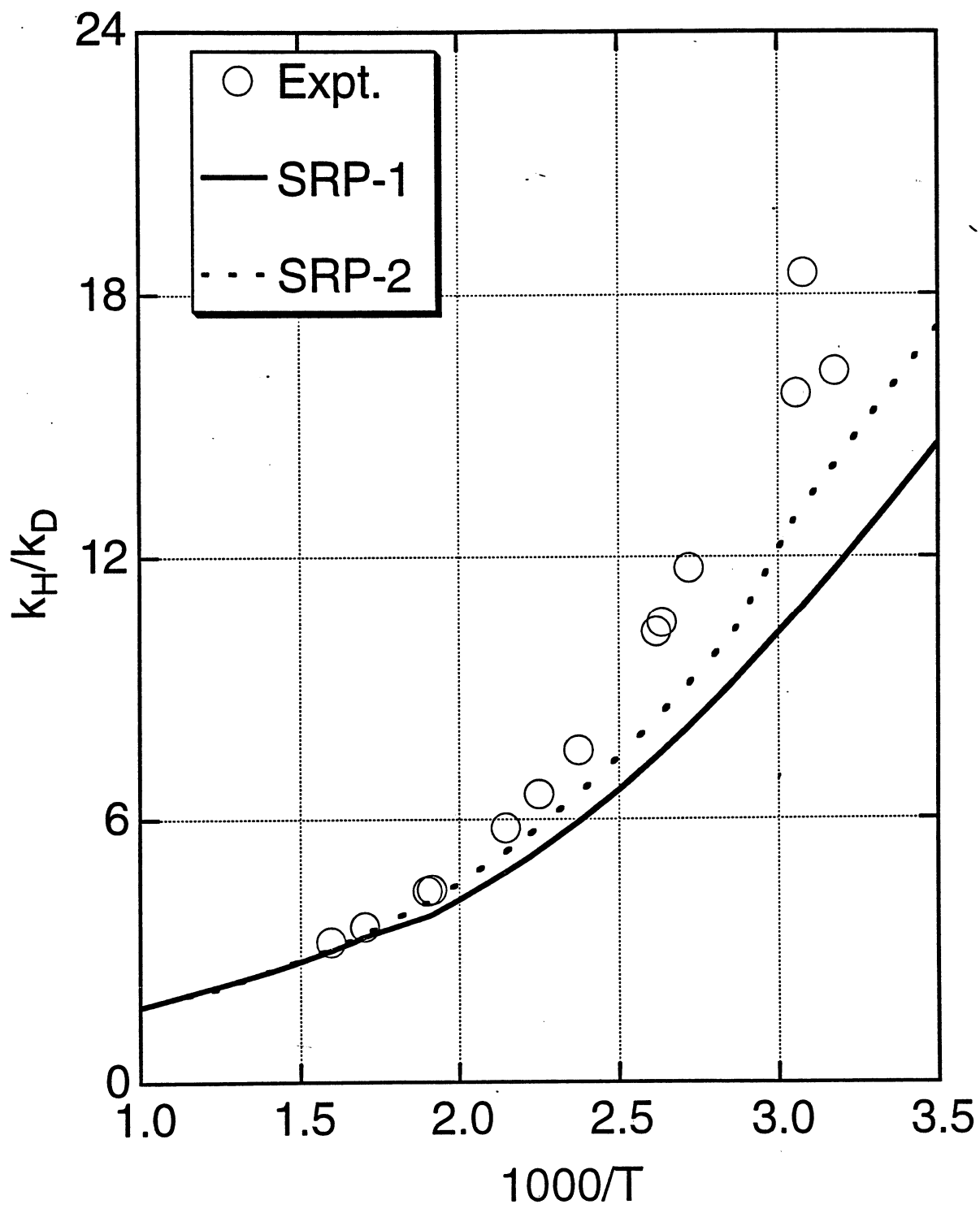


Figure 6

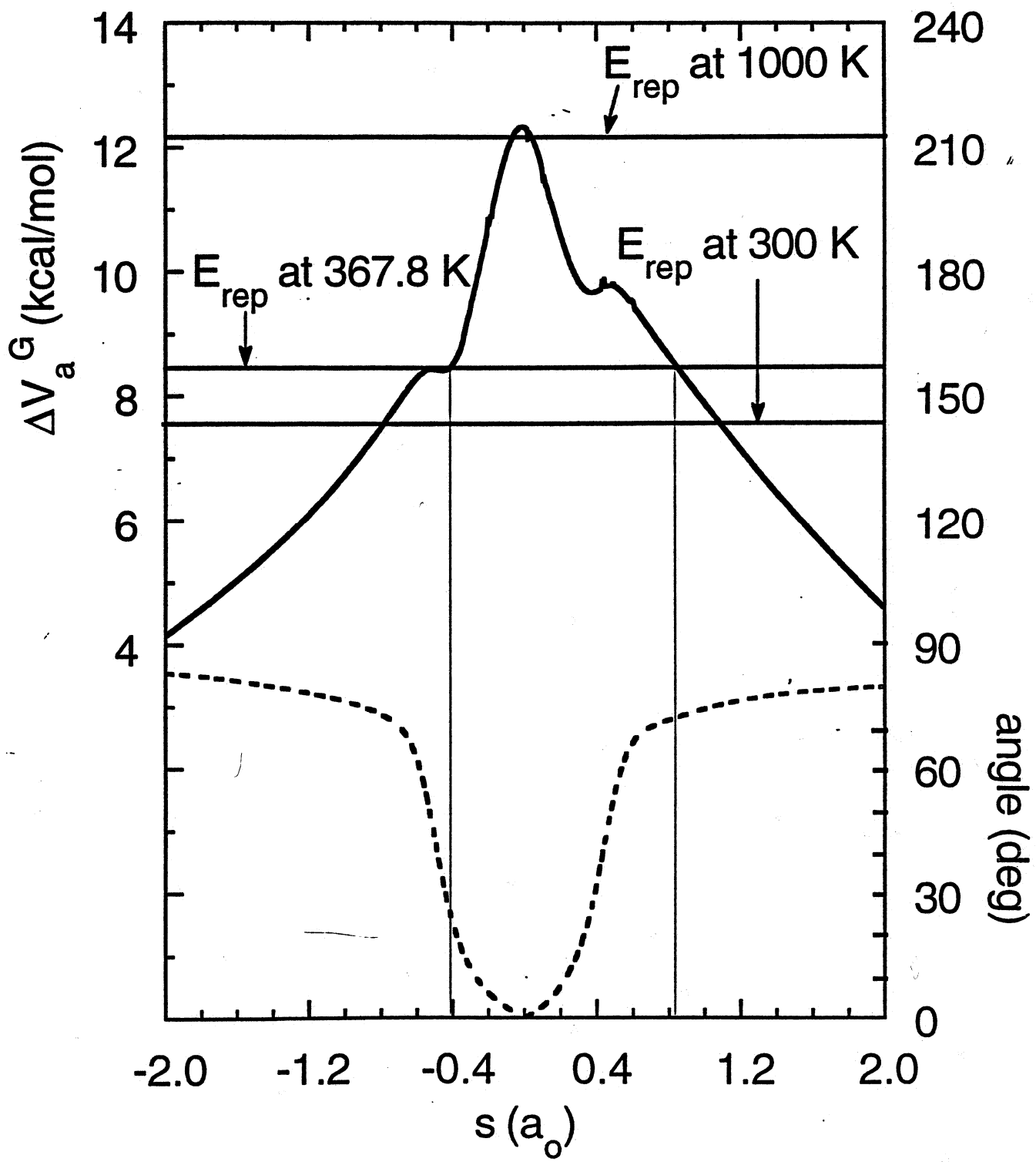


Figure 7

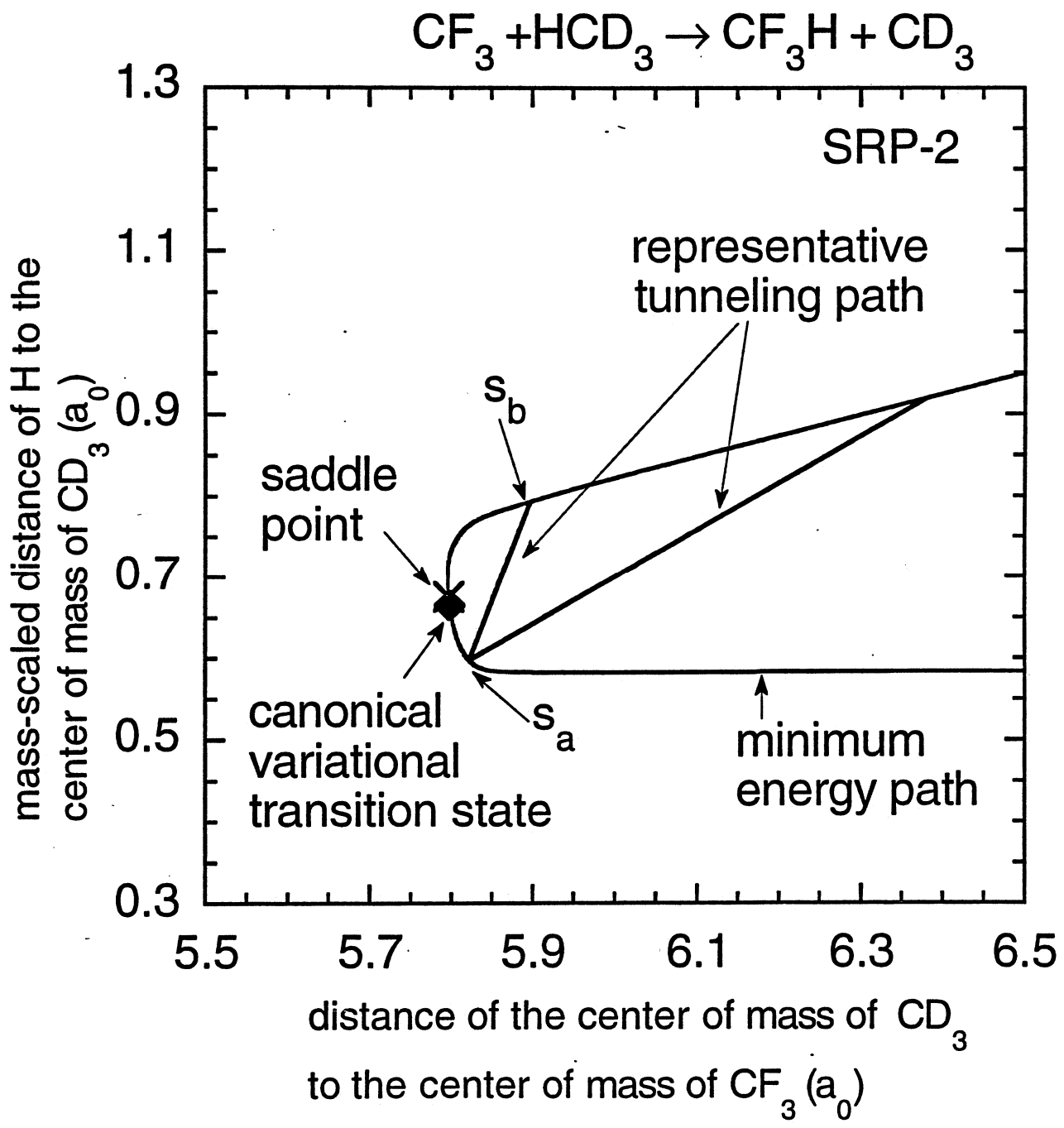


Figure 8

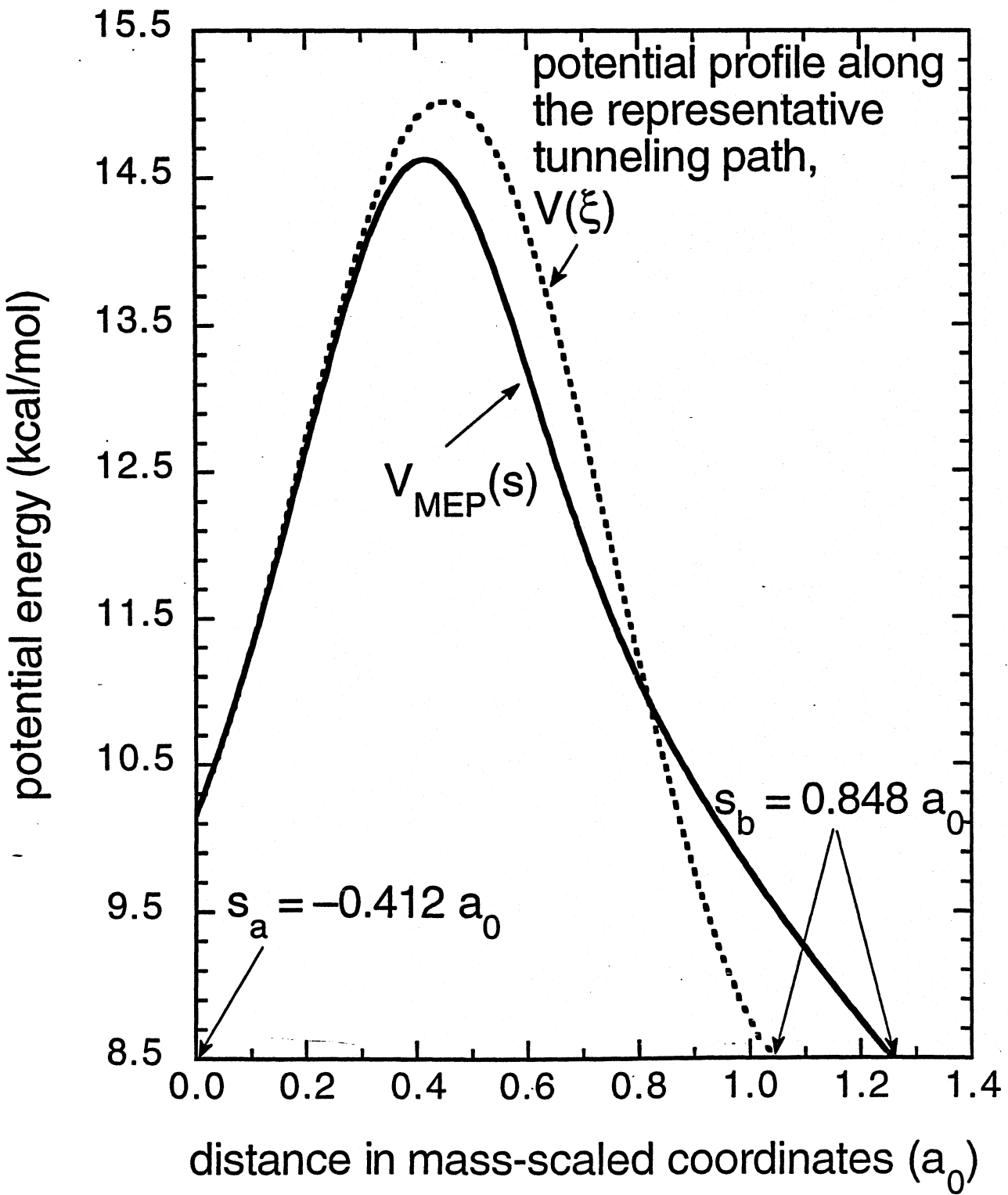


Figure 9

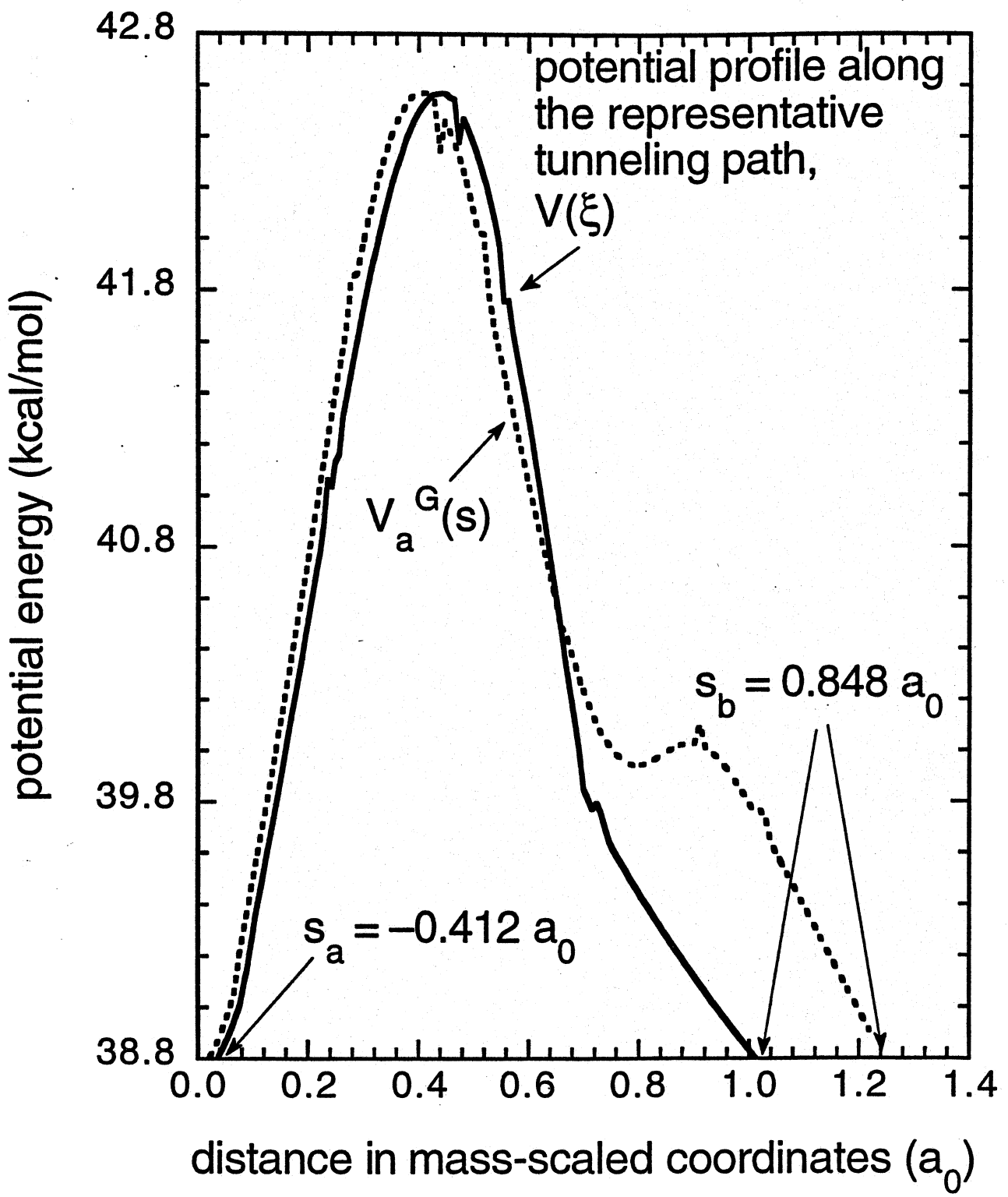


Figure 10